

A SEARCH FOR INTRINSIC HI 21 CM AND OH 18 CM ABSORPTION TOWARD COMPACT RADIO SOURCES

KATHRYN GRASHA^{1,2,3}, JEREMY DARLING³, ALBERTO BOLATTO⁴, ADAM K. LEROY⁵, JOHN T. STOCKE³

Draft version September 30, 2019

ABSTRACT

We present the results of a large search for intrinsic HI 21 cm and OH 18 cm absorption in 145 compact radio sources in the redshift range $0.02 < z < 3.8$ with the Green Bank Telescope. We re-detect HI 21 cm absorption toward six known absorption systems but detect no new HI or OH absorption in 102 interference-free sources. 79 sources have not previously been observed for HI 21 cm absorption. We recover a mean optical depth limit of $\tau_{3\sigma} < 0.023$ for all the non-detections in the survey. Our results do not support the high intrinsic absorption rates found by previous studies in compact radio sources at low redshift. Our results do, however, support the hypothesis proposed by Curran et al. (2008) that high ultraviolet (UV) luminosity active galactic nuclei (AGN) do not show intrinsic HI 21 cm absorption, confirming a threshold of $L_{\text{UV}} = 10^{23} \text{ W Hz}^{-1}$, above which our intrinsic absorption fraction is zero (54 sources). The exact nature of the UV luminosity effect on HI absorption systems remains ambiguous. We additionally find no statistical correlation between the 1.4 GHz radio luminosity or the source size and the 21 cm absorption detection rate. We attribute the lack of intrinsic absorption in our survey to the UV luminosity effect caused by an optical selection bias and a decreased column density sensitivity with increasing redshift due to lower radio continuum flux densities, high radio frequency interference, and higher telescope system temperatures at low frequencies.

Subject headings: radio lines: galaxies — quasars: absorption lines — galaxies: nuclei — galaxies: ISM — galaxies: active — galaxies: general

1. INTRODUCTION

Many compact radio sources are likely to be young and/or confined radio jets. It is likely that these very young and emerging jets are still contained within their host galaxy, potentially providing favorable sites to observe the interactions between the young, compact jets and the intrinsic gaseous interstellar medium (ISM) near the central active galactic nuclei (AGN) within their galaxies (O’Dea & Baum 1997; Owsianik & Conway 1998; Readhead et al. 1996).

One of the best observational tracers of the intrinsic ISM is with observations of the cold neutral medium (CNM) as traced by the hyperfine spin-flip transition of neutral hydrogen, the HI 21 cm line. When cold neutral hydrogen ($T \sim 100 \text{ K}$) is present, absorption of the 21 cm line against these compact radio sources gives the ability to detect neutral hydrogen absorption systems at any redshift. The 21 cm absorption line **could** thus be an invaluable probe of the kinematics and morphology of the neutral gas in the nuclear regions of galaxies. Studies of HI quite often employ the use of compact radio

sources as the best targets to detect 21 cm absorbers as the jets are still contained within their host galaxies, providing insight to the possible feedback interactions of these young jets with the neutral ambient medium.

Since the seminal work of Roberts (1970) that identified extragalactic associated HI 21 cm absorption in NGC 5128, a large number of HI 21 cm absorption studies have been carried out in an attempt to provide a better understanding of the properties of neutral gas, especially within compact radio source host galaxies. The discovery of blueshifted HI absorption systems at large velocities ($\gtrsim -1000 \text{ km s}^{-1}$; Vermeulen et al. 2003) with respect to the systemic optical redshift of the galaxy hosting the compact radio source is indicative of jet-driven outflows of neutral gas. This signifies a unique avenue in which to study the fueling of the AGN as well as the effects of AGN feedback and its interaction with the environment and gas kinematics of the host galaxy.

The majority of HI 21 cm absorption systems have high column density and are damped Ly α (DLA; $N_{\text{HI}} \geq 2 \times 10^{20} \text{ cm}^{-2}$) systems. The vast majority of 21 cm absorption systems have low redshifts, $z \lesssim 1$ (for a compiled literature list, see Curran et al. 2016) but some of intrinsic absorbers do lie above $z \gtrsim 1$ (Uson et al. 1991; Moore et al. 1999; Ishwara-Chandra et al. 2003; Curran et al. 2013; Aditya et al. 2017; Aditya & Kanekar 2018a). Previous surveys have identified a few commonalities exhibited in intrinsic HI 21 cm absorbers:

(1) High detection rates, of order 30-50%, are found in surveys of compact radio sources at redshift $z \lesssim 1$ (e.g., Vermeulen et al. 2003; Pihlström et al. 2003; Gupta et al. 2006; Geréb et al. 2015; Maccagni et al. 2017) whereas the detection rates in higher redshift surveys are signif-

¹ Research School of Astronomy and Astrophysics, Australian National University, Canberra, ACT 2611, Australia; kathryn.grasha@anu.edu.au

² ARC Centre of Excellence for All Sky Astrophysics in 3 Dimensions (ASTRO 3D), Australia

³ Center for Astrophysics and Space Astronomy, Department of Astrophysical and Planetary Sciences, University of Colorado, 389 UCB, Boulder, CO 80309-0389, USA

⁴ Department of Astronomy, University of Maryland, College Park, MD 20742-2421, USA

⁵ Department of Astronomy, The Ohio State University, McPherson Laboratory, 140 West 18th Avenue, Columbus, OH 43210-1173, USA

icantly lower (e.g., Kanekar & Chengalur 2003; Curran et al. 2008, 2011; Aditya et al. 2016, 2017; Curran et al. 2017; Moss et al. 2017). The deficiency of HI 21 cm absorbers at high redshift could arise from detection biases in sample selection or could signify physical changes in the reservoirs of cold neutral gas, AGN activity, or radio emission at earlier cosmic time (although neutral gas fractions are generally expected to increase with redshift; Rhee et al. 2018, and references therein).

(2) No intrinsic 21 cm absorption system has ever been detected toward objects with an ultraviolet (UV) luminosity $L_{\text{UV}} > 10^{23} \text{ W Hz}^{-1}$ (Curran et al. 2008, 2011, 2017) at any redshift. This luminosity is indicative of a UV bright, unobscured quasar with minimal extinction along the line of sight. While the exact nature of the UV luminosity's effect on neutral gas remains somewhat ambiguous, the observed threshold likely represents an analogue to the AGN "proximity effect" seen in UV absorption line studies (Bajtlik et al. 1988). The effect on the HI 21 cm absorption line could be the result of ionization of gas from the UV radiation (Curran et al. 2019), an increase in the spin temperature of the cold neutral medium (e.g., Kanekar & Chengalur 2003), effectively decreasing the observed line optical depth for a given column density, or simply identifying systems that are unextincted and have little gas and dust along the line of sight.

(3) High redshift, optically bright AGN are most likely to have spectroscopic redshifts. Most radio sources with spectroscopic redshifts beyond $z \sim 1.2$ have UV luminosities in excess of $L_{\text{UV}} > 10^{23} \text{ W Hz}^{-1}$. The UV luminosity threshold effect is therefore especially problematic for high redshift 21 cm absorption line detection because optical spectroscopic redshifts of AGN rely on rest-frame UV emission lines, biasing target selection toward the brightest UV sources that have never been detected in 21 cm absorption.

Another gas tracer that may be associated with neutral hydrogen absorption is the hydroxyl molecule (OH). OH shows absorption, emission, and maser activity in four hyperfine and lambda-doubled transitions at 18 cm. Cospatial HI and OH lines allow one to constrain the cosmic evolution of several physical constants: the electron-proton mass ratio $\mu \equiv m_p/m_e$, the fine structure constant $\alpha = e^2/\hbar c$, and the proton g-factor g_p (Chengalur & Kanekar 2003; Darling 2003, 2004; Kanekar & Chengalur 2004; Kanekar et al. 2005; Tzanavaris et al. 2005). The fine structure constant α parametrizes the strength of electromagnetic interactions, and some quasar studies suggest a decrease in α in the early universe (e.g., Cowie & Songaila 1995; Murphy et al. 2001; Darling 2004; Tzanavaris et al. 2007; Kanekar et al. 2006; Srikanth et al. 2010; Rahmani et al. 2012). Changes in the physical constants over cosmic time will cause spectral lines to shift from their relative measured values at present-day and have implications for physics and cosmology.

Redshifted OH systems are rarer than HI 21 cm absorption systems and are always found in systems that are detected in 21 cm absorption as well. Five OH 18 cm absorption line systems are known to date at $z > 0.2$ (Chengalur et al. 1999; Kanekar et al. 2003; Darling 2004; Kanekar et al. 2005, 2012), and none lie beyond

$z = 1$. Compact radio sources still confined within the host galaxy are the perfect environment to search for molecular systems, producing optimal conditions to observe OH absorption lines, especially the conjugate⁶ OH lines, systems in which OH gas complexes become sources of coupled weak maser emission and non-thermal absorption. Large surveys over a broad redshift range are required to detect the rare coincidence of HI 21 cm and OH 18 cm absorption lines.

In this paper, we perform a large survey for intrinsic HI 21 cm and OH 18 cm absorption in the host galaxies of 145 compact radio sources, including GHz-Peaked Spectrum (GPS), Compact Steep-Spectrum (CSS), Compact Symmetric Objects (CSOs), and Flat-Spectrum Radio Sources (FSRs); see Section 2 for further discussion of these classifications), using the Green Bank Telescope⁷ (GBT) selected across the redshift range ($0.02 < z < 3.8$) in an attempt to increase the number of known absorbers, especially at high redshift. In addition to the results of our search for intrinsic HI and OH absorption, we examine several biases that influence the detection of intrinsic absorption, including redshift selection, UV luminosity, radio luminosity, radio source size, covering factor, and spin temperature. We explore the possibility that the nature of our high redshift selection of radio sources biases the results against detection of intrinsic 21 cm absorption. Previous 21 cm absorption studies of the same biases we investigate here were performed on a heterogeneous compilation of previous known intrinsic HI absorption with a wide range of source sizes that were typically located at low redshift (e.g., Vermeulen et al. 2003; Gupta et al. 2006; Geréb et al. 2014). These results are arguably not unbiased because non-detections have generally not been uniformly published, which will skew the detection rates. We use this large survey to test the UV luminosity threshold hypothesis and the high rate of intrinsic HI 21 cm absorption toward compact radio sources.

The paper is outlined as follows. The compact radio source sample selection is described in Section 2 and their observations are described in Section 3. The results and comparison to previous 21 cm absorption searches are presented in Section 4. Section 5 presents the analysis of the HI detection rate with the radio and UV luminosities. We discuss the findings in Section 6 and we summarize the results and conclusions in Section 7.

Throughout this paper, we adopt a flat Λ CDM cosmology with $\Omega_m = 0.27$, $\Omega_\Lambda = 0.73$, and $H_0 = 71 \text{ km s}^{-1} \text{ Mpc}^{-1}$ (Komatsu et al. 2011). All quantities obtained from the literature are recalculated (if necessary) for this cosmology.

2. SAMPLE SELECTION

Compact radio sources are often classified by their morphology and radio spectral index, providing insight

⁶ The satellite OH conjugate lines (1612 and 1720 MHz) are a rare astrophysical phenomenon where the two lines have the same shape but opposite signs, arising due a population anti-inversion mechanism resulting from quantum mechanical selection rules (Elitzur 1992; van Langevelde et al. 1995; Darling 2004; Kanekar et al. 2018).

⁷ The National Radio Astronomy Observatory is a facility of the National Science Foundation operated under cooperative agreement by Associated Universities, Inc.

into the properties and nature of these sources. GHz-Peaked Spectrum (GPS) sources are intrinsically small (i.e., not foreshortened by projection effects; Fanti et al. 1990) and show a low frequency turn-over in their spectra, mainly attributed to synchrotron self-absorption and free-free (thermal bremsstrahlung) absorption (Jones et al. 1974; Menon 1983; O'Dea & Baum 1997). Compact Steep-Spectrum (CSS) sources show steeper power-law spectra than is typically seen in radio galaxies (Peacock & Wall 1982). Compact Symmetric Objects (CSOs) show a compact double-lobed structure with advance speeds, indicative of young jets (Wilkinson et al. 1994; Owsianik & Conway 1998). Flat-Spectrum Radio Sources (FSRSs) are characterized with a double-peaked synchrotron/Compton spectral energy distribution, possibly associated with a blazar or with the compact core of a radio galaxy (Fugmann 1988; Molina et al. 2012). These classifications are not disjoint in the literature; for example, most CSOs are also classified as GPS sources (Xiang et al. 2005).

Candidate intrinsic HI 21 cm absorbers in this survey include nearly all known GPS sources, CSS sources, and CSOs (ca. 2005) with $\delta > -35^\circ$ (Spencer et al. 1989; Fanti et al. 1990; de Vries, Barthel, & O'Dea 1997; Morganti et al. 1997; O'Dea & Baum 1997; Peck & Taylor 2000; Xiang et al. 2005) for a total of 60 objects (34 GPS sources, 29 CSS sources, and 7 CSOs, with some overlap between the classifications). The FSRSs were selected from White & Becker (1992) with $S > 0.3$ Jy at 780 MHz, adding an additional 85 sources to the sample selection.

In total, the sample includes 145 objects with known optical redshifts $0 < z < 4$, with the vast majority of the sample at redshifts less than $z \sim 1$. Figure 1 shows the redshift and the continuum flux density at the expected redshifted line frequency of the two samples (compact and flat-spectrum sources; Section 4.2). Table 1 lists the sources, their radio classifications (GPS, CSS, CSO, and FSRS), total integration time for each reduced spectrum.

3. OBSERVATIONS AND DATA REDUCTION

From September 2004 to August 2005, we observed 85 FSRSs for intrinsic absorption in the HI 21 cm line (1420.405752 MHz), and 81 in the four 18 cm OH lines at 1612.231, 1665.4018, 1667.35903, and 1720.5300 MHz simultaneously (GBT program 04C-018). We additionally observed 60 GPS, CSS, and CSO radio sources for intrinsic absorption from December 2005 to May 2006 (GBT program 06A-044): 59 sources were observed in the HI 21 cm line, and 44 sources were observed in the four OH 18 cm lines. One source, PKS 2135-209, was only observed in the OH lines. All observations were conducted using a 5-minute position-switched mode in two linear polarizations with 9-level sampling, 3- to 15-sec records, and a 50 MHz bandwidth centered at the redshift of the radio source host galaxy. Each bandwidth contains 4096 spectral channels with a width of 12.2 kHz per channel (a channel width of 3.86 km s^{-1} at $z = 0.5$). A calibration diode signal was injected for half of each record. Total on-source integration times were typically 30 minutes for the GPS, CSS, and CSO sources and 5 minutes for the FSRSs, listed in Table 1.

Each off-source-flattened and diode-calibrated spectral record was inspected and flagged for radio frequency

interference (RFI). All records were then averaged in time and polarization, Hanning smoothed, and baseline-flattened using a polynomial fit, typically of third order with a final post-smoothing spectral resolution of 24.4 kHz per channel. All data reduction was performed using GBTIDL⁸. Final mean spectra were inspected for absorption lines within a few thousand km s^{-1} of the optical redshift of the host galaxy. The observable velocity span was typically determined by the RFI conditions rather than the spectral bandwidth.

4. RESULTS

The nature of 36 sources (25% of the total sample) remains ambiguous due to unrecoverable contamination of RFI, a pernicious impediment to the detection of new absorption systems. The remaining 108 sources have the majority of their spectral range free from RFI and are able to be searched for HI or OH absorption.

Table 2 lists the RFI-free velocity range searched for HI 21 cm absorption toward each radio source, the measured rms noise (away from RFI and spectral lines) in the mean spectra, the continuum flux density at the expected frequency of the redshifted spectral line obtained from power-law fits to extant continuum measurements in the literature (see Section 4.2), HI column densities (or upper limits toward radio sources not detected in 21 cm absorption), and the projected size of each radio source as obtained from literature searches (see Section 5.3).

Table 3 lists the properties of the OH 18 cm line observations toward a subset of the sample. The 1665 and 1667 MHz lines are both observed, but we only list the properties of the 1667 MHz line because it places the strongest upper limit on the OH column density among the 18 cm lines. The continuum flux density is interpolated at the expected frequency of the redshifted 1667 MHz line from continuum measurements in the literature following the same method used for the 21 cm spectral observations (Section 4.2). When the 1667 MHz line could not be observed due to RFI, the 1612 or 1720 MHz transitions are used as the reference instead.

4.1. Line Detections and Limits

We detect intrinsic HI 21 cm absorption in 6 of the 108 RFI-free compact radio sources in our sample. The detection rate is 5.6%, substantially lower than in previous intrinsic HI absorption line surveys (Section 6). All of these absorption lines are detected in previous surveys (see Table 2 for references). The detected line spectra are shown in Figure 2, where velocities are referenced to the optical heliocentric redshift. Table 4 lists the measured and derived properties of the detected HI 21 cm absorption lines.

Table 2 lists the measured upper limits to the column densities, calculated according to Section 4.3.1 and further discussed in light of previous studies in Section 4.4.1. We show the spectra of the 102 RFI-free sources that show no significant HI 21 cm absorption lines and are predominately free from RFI in the Appendix.

⁸ GBTIDL (<http://gbtidl.nrao.edu/>) is the data reduction package produced by NRAO and written in the IDL language for the reduction of GBT data.

PKS 0742+10, at $z = 2.64$, shows a redshifted negative spectral feature with a signal to noise of 3.4σ . We compare our spectrum to that of Curran et al. (2013), also obtained at the GBT. The Curran et al. (2013) spectrum shows narrow RFI at the frequency of the potential absorption line. This suggests that the feature in our spectrum is likely to be an incompletely flagged or low-level RFI feature. We therefore treat PKS 0742+10 as a non-detection in all subsequent figures and statistics, with the rms noise measured away from the spectral feature.

None of the four 18 cm OH lines are detected in absorption or emission in 102 RFI-free spectra out of the 125 objects observed. Table 3 lists the properties of the OH sample, and Figure 15 in the Appendix shows the OH 1667 MHz non-detection spectra of the four 21 cm absorbers in our sample with RFI-free OH spectral observations.

4.2. Flux Densities

The nature of our observations with the GBT maximizes the on-time observation of targets and as a result does not give the necessary observations to flux calibrate the data and directly measure the continuum flux density. Moreover, for position-switched observations, RFI and instrumental effects frequently result in negative continuum values, artificial continuum slopes, and bandpass structure. The continuum is however paramount to obtain the optical depth and measure the column density or place a limit in the cases of non-detections (see eqn. 1). We therefore obtain the continuum flux density at the frequency of the redshifted HI and OH line of each source from an interpolation between extant continuum measurements in the NASA Extragalactic Database (NED) using a single spectral index power-law fit (a linear fit in $\log S_\nu - \log \nu$ space). In order to cope with the heterogeneous literature continuum measurements, we try whenever possible to select values published from the same catalogs and pass bands, most often observations at 1410, 1340, 750, 635, 408, and 365 MHz (Laing & Peacock 1980; Large et al. 1981; Ficarra, Grueff, & Tomassetti 1985; White & Becker 1992; Douglas et al. 1996; Rengelink et al. 1997; Stanghellini et al. 1998; Condon et al. 1998; Stanghellini et al. 2005; Orienti et al. 2007; Petrov et al. 2008). The uncertainties in the interpolated continuum flux densities listed in Tables 2 and 3 are obtained from estimates of the 1σ confidence intervals of the power law continuum fits for each object. This treatment neglects potentially significant time variation in radio source fluxes.

4.3. Column Densities

4.3.1. HI Column Density

Column densities are derived from the integrated optical depths of spectral lines. The column density associated with a given 21-cm line optical depth is calculated according to Wolfe & Burbidge (1975) as

$$N_{\text{HI}} = (1.8 \times 10^{18} \text{ cm}^2) \frac{T_s}{f} \int \tau \, dv, \quad (1)$$

where T_s is the spin temperature of the 21 cm line in Kelvin, f is the fraction of the area of the continuum source covered by the absorber, and $\int \tau \, dv$ is the optical depth τ integrated across the velocity span of the

line, in km s^{-1} , calculated from the continuum fluxes acquired in Section 4.2 and the strength of the absorption line. A Gaussian absorption profile can be integrated: $\int \tau \, dv = \sqrt{\pi / \ln 2} \tau_{\max} \Delta v / 2$, where τ_{\max} is the peak optical depth of a line with a full width half max (FWHM) of Δv . The column densities of the six re-detections of 21 cm absorption are calculated according to Eq. 1 and are listed in Table 4. We use both Gaussian fits and direct integration for the total HI column density of the 21 cm detections.

For the non-detections, we assume optically thin lines, and the 3σ upper limit on the column density can be approximated by

$$N_{\text{HI},3\sigma} < (1.9 \times 10^{18} \text{ cm}^{-2}) \frac{T_s}{f} \tau_{3\sigma} \Delta v, \quad (2)$$

where $\tau_{3\sigma} \approx 3\sigma/S$, σ is the rms noise, and S is the continuum flux density of the radio source at the redshifted line frequency.

All HI column densities are computed assuming $T_s = 100$ K and a uniform covering factor of $f = 1$, resulting in an HI column density limit in the CNM phase of the ISM. We note that this is not the total HI column density as the 21 cm transition is not a reliable tracer of the gas in WNM due to the optical depth inversely related to the spin temperature.

Non-detection column density limits assume $\Delta v = 30 \text{ km s}^{-1}$. Table 2 lists the column densities and limits for the non-detections and all upper limit spectra are shown in the Appendix. Figure 3 shows the HI column density distribution as a function of redshift for the 108 RFI-free sources.

4.3.2. OH Column Density

For the redshifted OH 18 cm line non-detections, we use the 1667 MHz OH transition to place the strongest upper limit on the OH column densities via

$$N_{\text{OH},3\sigma} < X \times 1.0645 \frac{T_x}{f} \tau_{3\sigma} \Delta v, \quad (3)$$

where $X = 2.38 \times 10^{14} \text{ cm}^{-2}$ (Curran et al. 2008) for the 1667 MHz transition, and T_x is the excitation temperature of the OH 1667 MHz line. When the 1667 MHz line could not be observed due to RFI, the OH column density limit is calculated using the 1612 MHz or 1720 MHz transition, which have $X = 2.14 \times 10^{15} \text{ cm}^{-2}$ ($X_{1612 \text{ MHz}} = 9 \times X_{1667 \text{ MHz}}$, following the 18 cm OH line ratios in thermodynamic equilibrium). We make no assumption about the OH line excitation temperatures and leave T_x as a free parameter in our tabulation and analysis. As with the HI lines, for the OH lines we assume a uniform covering factor of $f = 1$, and a line width of $\Delta v = 30 \text{ km s}^{-1}$. Figure 4 shows the OH column density limits as a function of redshift for the 102 RFI-free sources in the sample.

Because we find no OH detections, as well as no new HI detections, we are unable to place any meaningful constraint on possible redshift variations in the fundamental physical constants, discussed in Section 1.

4.4. Comparison to Previous Work

4.4.1. HI 21 cm Absorption Studies

This intrinsic HI 21 cm absorption search toward 144 compact radio sources (Table 1; one additional source is only observed for the four OH lines, for a total sample size of 145) obtained 108 spectra including six re-detections, with 36 sources remaining ambiguous due to RFI. 21 objects in the survey sample are previously observed for intrinsic HI absorption including nine known 21 cm line absorbers in the sample.

We made no new 21 cm absorption detections, however, we do re-detect six of the nine known HI absorption systems (Table 4). We are not able to re-detect the three absorption line systems toward 3C49, B3 1355+441 (Vermeulen et al. 2003) or 3C190 (Ishwara-Chandra et al. 2003) due to RFI.

Our spectra of 3C138, 3C147, 0239+108, OE+131, TXS 0902+490, HB89 0954+658, 1004+141, FBQS J1159+2914, 1418+546, 1642+690, 3C380, 4C+29.56, 2007+222, and PKS 2149+056 improves the previous upper limit measurements (Vermeulen et al. 2003; Carilli et al. 1998; Curran et al. 2017, 2019; Aditya & Kanekar 2018a,b). Three objects, B3 0248+430, SBS 0804+499, and 3C147, were impacted by RFI in our observations, preventing independent upper limits on previous measurements. Five sources, 3C138, HB89 0754+100, COINSJ 1546+0026, PKS 2121–01, and HB89 2342+821 have column density limits comparable to previous surveys. Only two limits on our sources, B2 0738+31 and COINS J2022+6136, did not improve on previously published column density limits. The remaining 79 sources have (to our knowledge) never been searched for intrinsic HI absorption before. Table 2 lists the column densities or column density limits from our survey and previous surveys along with references, if applicable. All non-detections quoted at the 3σ level use the assumptions listed in Section 4.3.

The six detected absorbers all have column densities near or greater than the DLA limit of $N_{\text{HI}} > 2 \times 10^{20} \text{ cm}^{-2}$ and we reached adequate sensitivity to have detected most known redshifted 21 cm absorbers if they had been present in our sample. 70% of our non-detections have 3σ upper limits below the DLA column density threshold for the detected absorbers. This suggests that while we have the sensitivity to detect new systems of cold gas ($T \sim 100 \text{ K}$) at sub-DLA column densities, there must be physical reasons for the dearth of absorption lines in these redshifts radio sources in this survey, which we investigate further in Section 5.2.

4.4.2. OH 18 cm Absorption Studies

We searched 125 radio sources for the four OH 18 cm lines, which can appear in either emission or absorption. The spectra of 102 objects are unaffected by RFI for at least one of the four OH transitions. No OH emission or absorption lines are detected in any of the RFI-free spectra and the OH column density upper limits are reported in Table 3. Only one source in our sample, B3 1355+441, has prior OH observations (Curran et al. 2006). We report a 3σ upper limit on the OH column density of $N_{\text{OH}}/T_x < 2.1 \times 10^{13} \text{ cm}^{-2} \text{ K}^{-1}$, an improvement over of the 3σ measurement of $N_{\text{OH}}/T_x < 11 \times 10^{13} \text{ cm}^{-2} \text{ K}^{-1}$ from Curran et al. (2006).

Four RFI-free OH observations toward known 21 cm absorbers (Figure 15) do not detect any OH lines despite reaching very low optical depths, $0.002 < \tau_{3\sigma} < 0.01$

(Table 3). OH column density upper limits for the full sample span the range $10^{12} \text{ cm}^{-2} \text{ K}^{-1} < N_{\text{OH}}/T_x < 10^{16} \text{ cm}^{-2} \text{ K}^{-1}$, consistent with upper limits quoted in previous surveys for non-detections of OH 18 cm absorption (Gupta et al. 2006; Curran et al. 2008, 2011).

5. ANALYSIS

We detect no new 21 cm absorption systems in our survey. We do, however, re-detect six known absorbers, for a detection rate of 5.6%. The following sections discuss factors that may negatively impact the ability to detect neutral HI gas, especially at high-redshift.

5.1. Radio Continuum Luminosity

One possible explanation of our low detection rate, especially at high redshift, is a high spin temperature. As shown in Equation 2, the measured HI column density is proportional to the (unknown) spin temperature T_s of the absorbing gas. Previous studies investigated the impact of the local radio radiation field in driving the spin temperature up in associated absorption systems (e.g., Gupta et al. 2006; Curran & Whiting 2010), finding little to no significance dependence of the radio luminosity on the detection rate or N_{HI} . If the spin temperature is coupled to the local radio radiation temperature, an increase would cause weaker line absorption for a given column density. However, recent work by Aditya & Kanekar (2018a,b) suggest that gas excitation from the radio continuum may be responsible for the dearth of 21-cm absorbers detected at high redshift. This suggests that the spin temperature of the gas, a measure of the excitation from the lower hyperfine level (Field 1959), can be raised by excitation to the upper hyperfine level by rest-frame 1420 MHz photons. Curran et al. (2019) has shown that this is unlikely and that the photoionization from the UV luminosity is dominant factor over the radio luminosity in negatively impacting the detection rate of 21 cm absorbers (see Section 5.2).

We test this possibility of the impact of the incident 21 cm luminosity on the absorption detection rate by calculating the specific radio continuum luminosity in the vicinity of the 21 cm line in the rest frame of each host galaxy (van Gorkom et al. 1989):

$$L_\nu = \frac{4\pi D_L^2 S_\nu}{1+z} \text{ W Hz}^{-1}, \quad (4)$$

where D_L is the luminosity distance of the host galaxy, S_ν is the observed 21 cm flux density at the frequency of the redshifted 21 cm observations, as calculated in Section 4 and listed in Table 2, and z is the redshift.

Table 5 lists the radio continuum luminosities for the sample. The median radio continuum luminosity of the detections is $\log(L_{\text{Radio}}/\text{W Hz}^{-1}) = 27.5 \pm 0.4$, consistent with the median luminosity for the non-detections at 27.5 ± 0.7 . A Kolmogorov-Smirnov Test (KS-test) shows that the 21 cm rest-frame luminosity differs between the detections and non-detections at less than 1σ confidence level; the 21 cm luminosity does not appear to be a major factor in 21 cm absorption and cannot explain our low detection rate, also found in Curran & Whiting (2010).

With the exception of a few low-luminosity radio sources, the radio luminosity-redshift distribution shows

the Malmquist bias for flux-limited surveys: the most luminous objects lie at the largest distances (Figure 5). As expected, the detections show an inverse correlation of radio luminosity with column density (Figure 6). This, however, is an observational bias because the highest flux density sources typically have the highest luminosities (Figure 5), and high flux densities provide greater column density sensitivity.

5.2. Ultraviolet Luminosity

Another possible explanation for this survey’s lack of intrinsic 21 cm absorption at high redshift is the hypothesis proposed by Curran et al. (2008) that AGN with a high ultraviolet ($\lambda_{\text{UV}} = 1216 \text{ \AA}$) luminosity ($L_{\text{UV}} > 10^{23} \text{ W Hz}^{-1}$) may inhibit 21 cm absorption. If the UV flux of the central AGN is sufficient to ionize (or simply heat) the neutral gas within the host galaxy, UV-bright galaxies will be biased against the detection of 21 cm absorbers. These UV bright sources are also likely to be unextincted and may simply have less gas and dust along the line of sight compared to extinguished sources, lowering the ability to detect absorption systems as sensitivity depends on both the covering fraction of the gas against the background source and the spin temperature of the gas. The UV luminosity bias will be compounded with increasing redshift because flux-limited surveys will naturally select UV-luminous objects at all redshifts.

We have searched the literature for optical and near-IR photometry of each source in our sample to estimate the rest-frame UV luminosity following the method in Curran et al. (2008). Table 5 lists the optical and near-IR magnitudes for the sources searched for 21 cm absorption. Of our detected absorbers, 4C+76.03 does not have adequate available optical or near-IR observations. For this source, along with six sources with non-detections, we are unable to estimate the UV-optical slope in order to measure the expected UV luminosity. We therefore do not calculate a UV luminosity for these sources and they have been excluded from all plots and analysis related to the UV luminosity. In conclusion, we have five detections in 21 cm absorption and 96 sources with upper limits that we are able to calculate a UV luminosity for in order to test the hypothesis proposed by Curran et al. (2008) for the ionization of the atomic gas in UV-bright radio sources.

Using visible band magnitudes and attempting to maintain consistency in the heterogeneous sample and sources of magnitudes, the extrapolation or interpolation of the rest-frame UV luminosity at 1216 Å is performed using a power-law fit to the B and R bands as these two bands are readily available for most for the sample. For sources where either of those bands are not available, observations at V or K bands are substituted in that order. We require a minimum of two bands to perform the power-law fit, for galaxies with more than two available magnitudes, we use all available optical and near-IR bands. Objects with Sloan Digital Sky Survey (SDSS) $u'g'r'i'z'$ magnitudes are converted to Johnson magnitudes using the methods described in Smith et al. (2002) and are not corrected for intrinsic source extinction.

The fitting is done by converting the visible band magnitudes to fluxes using Vega as a zero-point reference, with values for Vega in each band taken from

Bessell (1979), Campins et al. (1985), and Schneider et al. (1983). Under the assumption that a single power law applies from the observed optical wavelengths down to 1216 Å, the UV flux density in the rest-frame of the host galaxy is obtained from the observed flux F_1 at wavelength λ_1 from Curran et al. (2008) as,

$$F_{\lambda_{\text{UV}}(1+z)} = F_1 \left[\frac{\lambda_{\text{UV}} (1+z)}{\lambda_1} \right]^\alpha, \quad (5)$$

where the spectral index α is estimated as $\alpha = \log(F_2/F_1)/\log(\lambda_2/\lambda_1)$ for two observations at bands λ_1 and λ_2 , with fluxes F_1 and F_2 . This allows us to extrapolate from the observed visible-band photometry to obtain a UV flux at the observed wavelength $\lambda_{\text{UV}}(1+z)$. The specific UV luminosity in the rest-frame of the host galaxy is then calculated as,

$$L_{\lambda_{\text{UV}}} = \frac{4\pi D_L^2 F_{\lambda_{\text{UV}}(1+z)}}{1+z} \text{ W Hz}^{-1}, \quad (6)$$

where D_L is the luminosity distance to the host galaxy and $F_{\lambda_{\text{UV}}(1+z)}$ is the rest-frame UV flux calculated from Eq. 5.

The median and 1σ values of the UV luminosity of the full sample of 101 sources (5 detections, 96 non-detections, 7 sources with no LUV measurement) is $\log(L_{\text{UV}}/\text{W Hz}^{-1}) = 23.1 \pm 1.4$, consistent with the UV luminosity threshold of $10^{23} \text{ W Hz}^{-1}$. The median luminosity of the HI absorption detections is $\log(L_{\text{UV}}/\text{W Hz}^{-1}) = 20.5 \pm 1.1$, and the median luminosity of the non-detections is $\log(L_{\text{UV}}/\text{W Hz}^{-1}) = 23.2 \pm 1.4$. If we only consider systems below the $L_{\text{UV}} < 10^{23} \text{ W Hz}^{-1}$ threshold, this reduces the number of RFI-free sources searched for 21 cm absorption from 101 to 47 targets. The detection rate for this subset of UV-faint sources increases to 9.8%.

Figure 7 shows the distribution of the HI column density as a function UV luminosity. There are no HI 21 cm line absorbers associated with sources with UV luminosities above $\log(L_{\text{UV}}/\text{W Hz}^{-1}) > 23$, further supporting the critical UV threshold above which 21 cm absorbers cannot be detected (Curran & Whiting 2010; Curran et al. 2017). Figure 8 shows the UV luminosity as a function of redshift, demonstrating how the radio sources in this survey above a redshift of $z \sim 1$ predominately have UV luminosities that are above the threshold. The requirement of UV/optical spectroscopic redshifts for radio spectral line surveys typically cause the high redshift sources to be the most luminous and are not ideal targets to show 21 cm or molecular absorption.

A KS-test comparing UV luminosities of the 21 cm detections to the non-detections, however, is not statistically significant, showing a 2.2σ difference between the samples. While the detections and non-detections do not appear to be drawn from distinct populations in UV luminosity, our sample of detections may simply be too small for statistical significance.

Figure 9 shows the radio versus UV luminosities of the sample with a Pearson correlation coefficient of $r = 0.35$, significant at the 3.7σ level. As with all luminosity-luminosity plots of flux-limited samples, some degree of correlation can arise from the correlation of both luminosities with distance. Figure 10 shows the measured

column density (or 3σ upper limits) versus the ratio of the radio-to-UV luminosity. The five HI 21 cm absorbers have a weak preference to be located in objects that have a higher than median ratio, indicating their preference to reside in sources with low UV luminosity and/or higher radio luminosity compared to the non-detected sources. A KS test results in a D-value of 0.677, significant at 3.2σ . Future work with a larger number of detections will be able to further investigate the effect of the UV and radio luminosities on cold gas, especially investigating preference for 21 cm absorption in UV-faint, radio-loud sources.

5.3. Physical Size

The size of the radio source may also influence the detection of HI 21 cm absorption. If the radio lobes predominately reside outside of the host galaxy, then the HI covering fraction will be small, and the apparent 21 cm optical depth will be correspondingly diminished.

The sizes of the radio sources in our survey are compiled from existing literature (Table 2). Physical and projected sizes are calculated using the angular size distance for each redshift. Projection (and presumably relativistic beaming) can confuse analysis and interpretation because not all sources with small projected linear sizes are physically small and vice versa (see, e.g., Fanti et al. 1989).

Figure 11 shows the HI column densities (upper limits in the case of non-detections) as a function of the projected linear size of the radio source. The detection of absorption systems does not seem to depend on source size and we find no correlation between the column density and the size of the source (Pearson correlation coefficient of -0.31). The detection rates among the larger sources (> 1 kpc; 2 out of 21 sources) and the smaller sources (< 1 kpc; 4 out of 87 sources) are consistent with each other.

Figure 12 shows that UV luminosity does not correlate with source size (correlation coefficient of $r = 0.14$, non-significant at 1.4σ). Among the detections, the larger sources do exhibit a higher UV luminosity ($L_{\text{UV}} > 10^{22.5} \text{ W Hz}^{-1}$) than the smaller sources ($L_{\text{UV}} < 10^{21} \text{ W Hz}^{-1}$), but the correlation is not statistically significant for a sample of five detections. Among non-detections, smaller sources (≤ 1 kpc) show a median UV luminosity of $\log L_{\text{UV}} = 23.0 \pm 1.3 \text{ W Hz}^{-1}$, consistent with that of the larger sources (> 1 kpc) with a median of $\log L_{\text{UV}} = 22.6 \pm 1.5 \text{ W Hz}^{-1}$. The median UV luminosities likewise do not differ among radio source classification types: the median UV luminosity of the GPS, CSS, and CSO sources is $\log L_{\text{UV}} = 22.8 \pm 1.6 \text{ W Hz}^{-1}$, while for FSRSSs, the median value is $\log L_{\text{UV}} = 23.1 \pm 1.2 \text{ W Hz}^{-1}$.

Figure 13 shows the relation between the radio continuum flux density and linear size of the radio jets, where the smallest radio sources tend to also be the faintest. These properties are countervailing in terms of the HI 21 cm absorption line detectability. Column density sensitivity increases toward brighter objects, which tend to occur in the largest radio sources. However, the largest radio sources are the most evolved (thus possibly residing in galaxies with less neutral gas) and most likely have the smallest covering fraction if the radio lobes are

located outside the galaxy, reducing sensitivity for systems with lower column densities. We do not find that smaller sources have a higher rate of detection in 21 cm absorption, instead, we find that the detected absorbers cover the full range of jet sizes available in the survey, concluding that the size of the radio source is not a main contributor against the detection of HI 21 cm absorption.

6. DISCUSSION

Some of the first surveys toward compact radio sources revealed intrinsic HI 21 cm detection rates of 30-60% in low redshift radio galaxies (Morganti et al. 2001; Pihlström et al. 2003; Vermeulen et al. 2003; Gupta et al. 2006). These previous surveys measure typical optical depth limits of $\tau_{3\sigma} \lesssim 0.001 - 0.2$ for non-detections. We recover a mean optical depth limit of $\tau_{3\sigma} < 0.023$ for our non-detections with a broad range from $10^{-6} < \tau_{3\sigma} < 0.15$, where 70% of the non-detections lie below the DLA column density threshold. For sources in our survey that were also present in previous studies, we typically achieve greater sensitivity and are able to improve prior upper limits.

The high success rate of 21 cm absorbers in these low- z studies have triggered follow up surveys to target compact radio sources in attempt to increase the detection rate of 21 cm absorption systems. The high success rates of these low-redshift surveys are in stark contrast, however, with surveys aimed toward high redshift $z \gtrsim 1$ targets, where the detection rate plummets to single digits (Curran et al. 2008; Aditya et al. 2016; Curran et al. 2017), hinting at a connection between the redshift of the source and the success of detecting 21 cm absorption lines. While our sources span the redshift range $0.2 < z < 3.8$, 75% of our RFI-free sample lie at redshifts $z < 1$ and we recover a detection rate of less than 6%, with all absorbers identified in prior surveys. Lack of new detections, especially at low redshift, while reaching the sensitivity to re-detect known absorbers, demonstrates that there have to be external physical factors at play that negatively impact the detection rate of neutral gas absorbers in our sample.

It is becoming clear that absorption of cold, neutral gas within galaxies that host radio sources is a multi-faceted problem, with many factors impacting the detection rate of HI 21 cm absorption, especially at high redshift. Different effects may influence each other and work together, such as the observed anti-correlation of the HI column densities with size of the radio source (Curran et al. 2013; Geréb et al. 2015). We do not recover the same correlation, although our data are not inconsistent with a decrease in the HI column density with increase in source size (Figure 11). Our results are limited by an extremely small number of detections. Surveys such as this one, even with such a large non-detection rate, across a range of parameters (e.g., redshift, column density, UV/radio luminosity, radio source size) marks an attempt to better test and constrain the multitude of factors that impact the gas reservoirs and will allow for a more comprehensive understanding of the physical, kinematic, and chemical properties of the neutral gas in the AGN environment.

Our low detection rate does not allow us to disentangle high (or even low) redshift biases against detection of 21 cm absorption. It is now clear that targeting UV-

bright quasars, a condition imposed to reliably constrain the redshift of the source using the rest-frame UV continuum, are not identifying targets with large enough reservoirs of cold, neutral gas detectable with large radio surveys such as this study. Future surveys should be designed to target highly extincted, obscured sources that are not bright in the UV. Such surveys can leverage the infrared capabilities from WFIRST or even JWST to serendipitously detect potential HI targets that are UV/optical faint but bright in the mid-IR (e.g., Yan et al. 2012, 2016). The SKA and its pathfinders will undoubtedly inaugurate a new era in HI absorption surveys, owing to large instantaneous bandwidth coverage and field of view. The improved sensitivity and spectral coverage achievable with the SKA will overcome observational biases introduced by the conventional requirement of an optical redshift, ushering in a future of true “blind” HI absorption surveys.

7. CONCLUSIONS

We present the results of the largest survey to date to search for intrinsic HI 21 cm and OH 18 cm absorption at redshifts between $0.02 < z < 3.8$ in 145 radio sources with the Green Bank Telescope. Below we summarize the major findings of this study.

1. Despite having the sensitivity to re-detect six previous detections of associated HI 21 cm absorption in our sample, we make no new detections of 21 cm absorption in the 108 sources for which we have RFI-free spectra. The overall HI 21 cm absorption detection rate is 5.6%, but no detections are made for $z > 0.7$. This is significantly lower than similar low redshift surveys.
2. We place an upper limit on the column density for all non-detections not affected by RFI, reaching a mean optical depth of $\tau_{3\sigma} < 0.023$. 79 of the radio sources have never been observed for HI 21 cm before. Despite low flux density values at the frequency of our redshifted 21 cm spectral observations, coupled with the significant presence of RFI in our low-frequency spectral observations, we reached adequate sensitivity to detect nearly any damped Ly α system.
3. We have searched 125 of our sources for intrinsic molecular OH 18 cm absorption. We do not detect any of the four OH lines in the 102 RFI-free sources for which we have usable OH data, obtaining exclusively upper limits for all measured OH column densities. We do not detect OH toward five of the known 21 cm absorption systems for which we have spectra coverage. Lack of OH absorption in these systems is not a result of insensitive measurements and we place upper limits on the OH column that are consistent with previously detected OH absorption systems.
4. We find no HI 21 cm absorption above an ultra-violet luminosity of $L_{UV} \gtrsim 10^{23} \text{ W Hz}^{-1}$. This supports the hypothesis that intrinsic 21 cm absorption cannot be detected in galaxies when the UV luminosity exceeds this UV luminosity threshold (Curran et al. 2008). Lack of 21 cm absorption

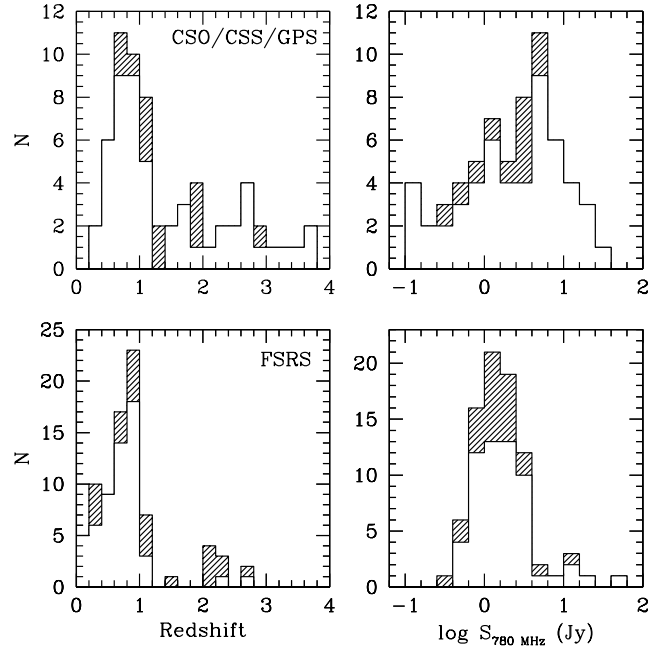


Figure 1. Redshift (left) and continuum flux density at the expected redshifted 21 cm line frequency (right) for the CSO, CSS, and GPS sources (top row) and the FSRSSs (bottom row) in our sample. The hatched cells show the objects that could not be observed for spectral lines due to RFI.

in UV bright sources is an effect due to either the ionization of the neutral gas, higher spin temperatures in the environment around these luminous AGN, or sources that simply do not have a sufficient column of cold, neutral HI along the line of sight.

5. We do not find statistically significant evidence that the HI column density of 21 cm systems in our sample depends on the radio jet size, UV luminosity, or radio (1.4 GHz) luminosity. We are limited, however, by small numbers.
6. With the exception of a single source, all of our RFI-free sources beyond $z \sim 1.2$ arise in UV-luminous sources above the UV luminosity threshold of $L_{UV} = 10^{23} \text{ W Hz}^{-1}$. This suggests that a possible explanation that the dearth of intrinsic 21 cm absorption systems at high redshift is an selection bias favoring UV-luminous AGN. Requiring optical redshifts (rest-frame UV for $z \gtrsim 1.6$) imposes an optical bias and low-dust column, selecting the brightest, least obscured, and UV-bright radio sources at all redshifts. Such sources create an environment where neutral gas cannot survive and as such, are not detectable in 21 cm absorption.

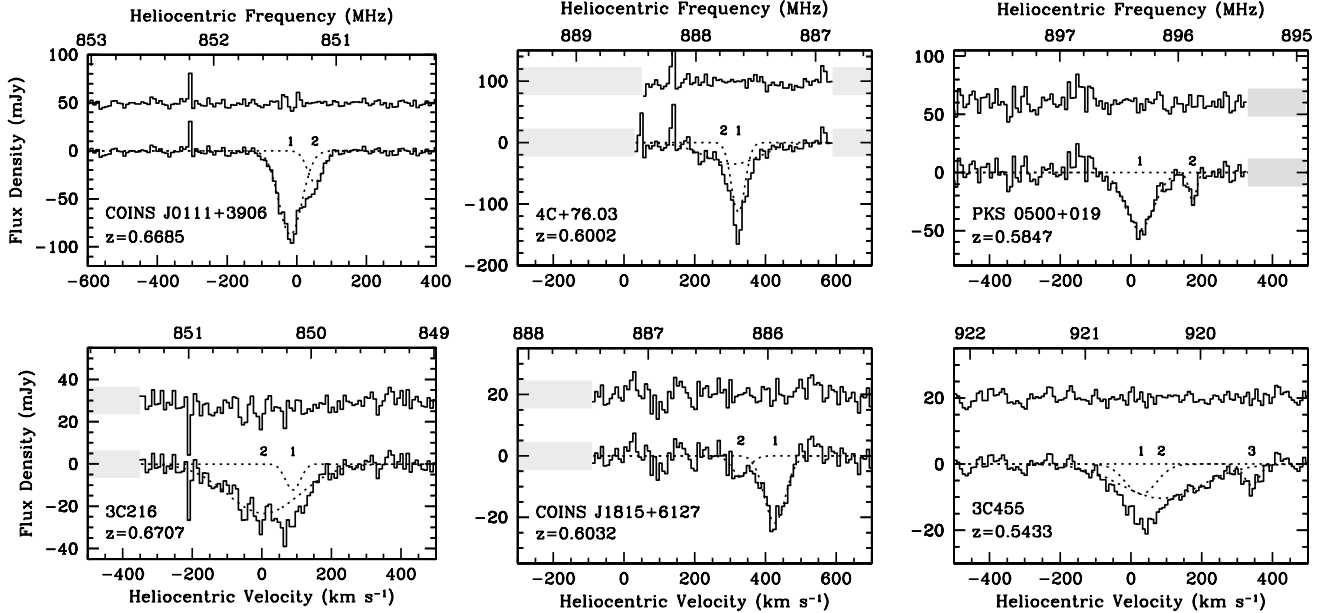


Figure 2. Intrinsic HI 21 cm absorption line systems. Dotted lines indicate Gaussian fits, numbered by component listed in Table 4. Upper spectra show the residual spectrum, offset for clarity. The velocity scale is in the rest frame of each object, defined by the optical heliocentric redshift of each radio source (Table 1). Spectral regions lost to radio frequency interference are greyed out.

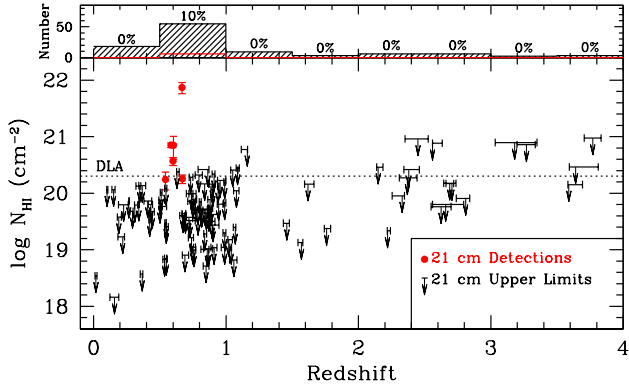


Figure 3. HI column density versus redshift. The lower panel shows either the detected HI column density at the redshift of the detected 21 cm absorption line or its 3σ upper limit in the case of non-detections. The horizontal bar on the 21 cm non-detections indicates the redshift search region, and the downward-pointing arrow is centered on the systemic redshift of each object; the 21 cm line search regions are generally determined by RFI conditions. The solid red points represent sources detected in 21 cm absorption with the 1σ error in the measured column density shown with the vertical error bars. The horizontal dotted line indicates the fiducial threshold for damped Ly α systems (DLAs; $N_{\text{HI}} \geq 2 \times 10^{20} \text{ cm}^{-2}$). The upper panel indicates the number of objects surveyed in each $\Delta z = 0.5$ redshift bin (black, hatched histogram), the number of intrinsic HI 21 cm absorption lines detected (red histogram), and the 21 cm absorption fraction (text percentages above each bin).

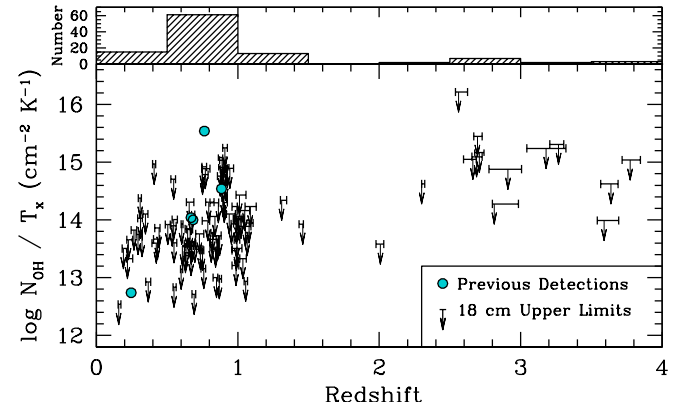


Figure 4. The lower panel shows the 3σ upper limit OH column density versus the optical redshift. The horizontal bar indicates the redshift search region, typically determined by RFI conditions, and the downward-pointing arrow is centered on the systemic redshift of each object. The upper panel indicates the number of objects surveyed in each $\Delta z = 0.5$ redshift bin (black, hatched). We show previous OH 1665 MHz absorption detections as teal symbols.

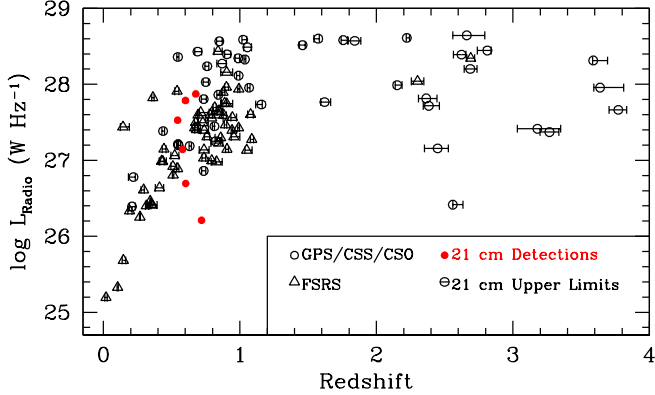


Figure 5. Radio luminosity versus redshift for RFI-free sources. We use the optical redshift for sources not detected in 21 cm and the absorption redshift for the six 21 cm detections. The horizontal bar on the 21 cm non-detections indicates the redshift search region for each source, generally determined by the RFI conditions. The solid red symbols represent 21 cm detections and unfilled black symbols represent the non-detections. The shape of the symbols represent the radio source identification: circles represent GPS, CSS, and CSO sources, and triangles represent FSRSSs.

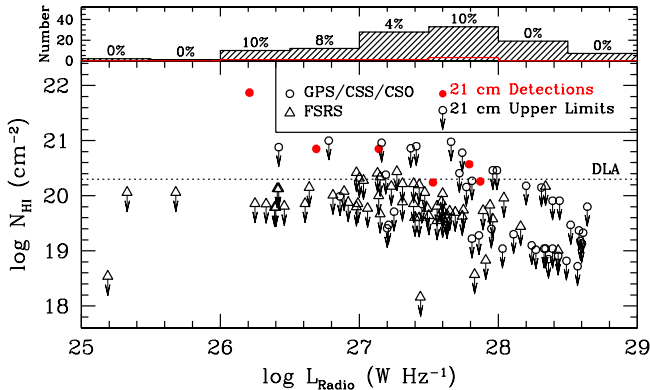


Figure 6. The lower panel shows the HI column density (upper limit in the case of non-detections) as a function of the specific radio luminosity. The horizontal dotted line indicates the canonical threshold for DLA systems. The solid red symbols represent 21 cm detections and unfilled symbols represent the non-detections. The shape of the symbols represent the radio source identification: circles represent GPS, CSS, and CSO sources, and triangles represent FSRSSs. The upper panel indicates the total number of objects surveyed in each $\Delta L_{\text{Radio}} = 0.5$ dex bin (black, hatched histogram), the number of intrinsic HI 21 cm absorption lines detected (red histogram), and the 21 cm absorption fraction (text percentages above each bin).

We are grateful for the valuable comments on this work by an anonymous referee that improved the scientific outcome and quality of the paper. The authors thank T. Yan and K. Willett for data reduction scripts. The authors thank the staff members at the Green Bank Telescope for their assistance and support. This research has made use of the NASA/IPAC Extragalactic Database (NED) which is operated by the Jet Propulsion Laboratory, California Institute of Technology, under contract with NASA. This publication makes use of data products from the Two Micron All Sky Survey, which is a joint project of the University of Massachusetts and the Infrared Processing and Analysis Center/California Institute of Technology, funded by the National Aeronautics and Space Administration and the National Science

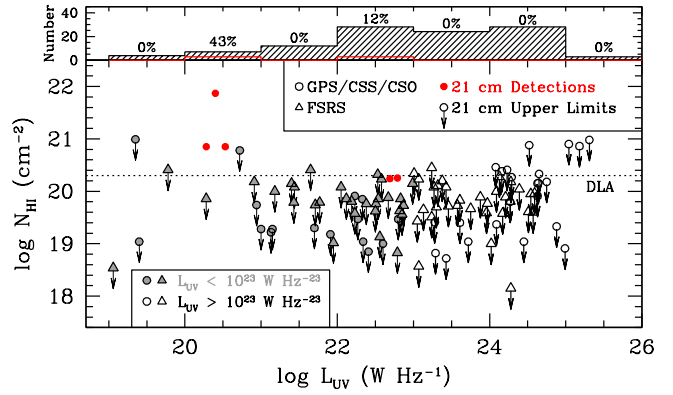


Figure 7. HI column density N_{HI} (upper limit for sources not detected in 21 cm absorption) as a function of the ultraviolet luminosity (Section 5.2). The horizontal dotted line indicates the threshold for DLAs. The solid red symbols represent 21 cm detections and downward pointing arrows are the upper limits for non-detections. Filled gray symbols represent the non-detections that are below the UV threshold of $10^{23} \text{ W Hz}^{-1}$ and open symbols represent the non-detections that are above the UV threshold. The shape of the symbols represent the radio source identification: circles represent GPS, CSS and CSO sources and triangles represent FSRSSs. The upper panel indicates the total number of objects surveyed in each $\Delta L_{\text{UV}} = 1$ dex luminosity bin (black, hatched histogram), the number of intrinsic HI 21 cm absorption lines detected (red histogram), and the 21 cm absorption fraction (text percentages above each bin). We confirm the findings of Curran et al. (2008) that 21 cm absorption is not detected in sources with a UV luminosity above the threshold of $10^{23} \text{ W Hz}^{-1}$. However, we detect no new absorbers in the sample below this UV luminosity threshold.

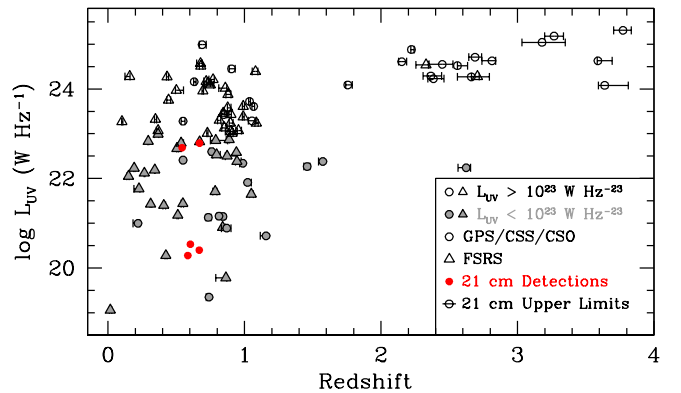


Figure 8. UV luminosity versus redshift for our RFI-free sources. We use the optical redshift for sources not detected in 21 cm and the absorption redshift for the five 21 cm detections with a measured UV luminosity. The horizontal bar on the 21 cm non-detections indicates the redshift search region for each source, generally determined by the RFI conditions. The solid red symbols represent 21 cm detections and unfilled black symbols represent the non-detections. The shape of the symbols represent the radio source identification: circles represent GPS, CSS, and CSO sources and triangles represent FSRSSs. 21 cm absorption systems have never been detected in sources with a UV luminosity above a threshold of $10^{23} \text{ W Hz}^{-1}$. This figure demonstrates the difficulty in selecting sources below the UV luminosity threshold (filled gray symbols) at redshifts above $z \sim 1$ that may possibly host 21 cm absorbers.

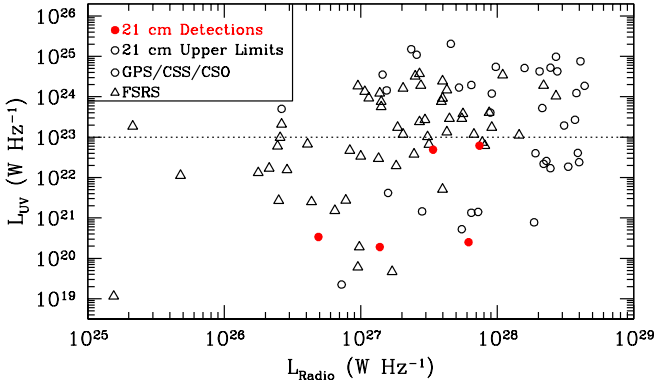


Figure 9. Ultraviolet luminosity versus radio continuum luminosity at the frequency of the redshifted 21 cm line. The solid red symbols represent 21 cm detections and unfilled black symbols represent non-detections. The shape of the symbols represent the radio source identification: circles represent GPS, CSS, and CSO sources and triangles represent FSRSs. The horizontal dotted line indicates the UV luminosity threshold ($L_{\text{UV}} = 10^{23} \text{ W Hz}^{-1}$) above which 21 cm absorption has not been detected.

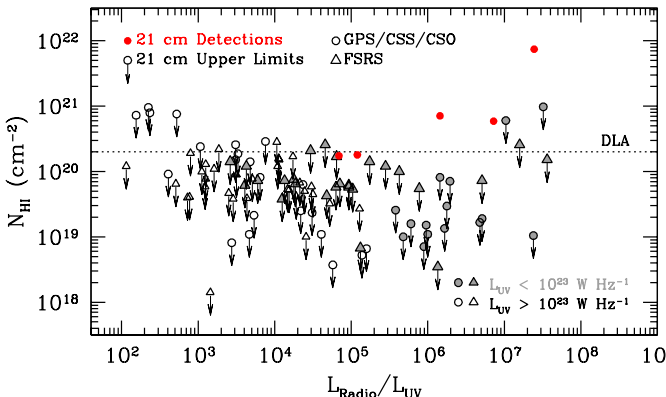


Figure 10. HI column density (upper limit for sources not detected in 21 cm absorption) versus the ratio of the radio to the UV luminosity (or flux density). The filled gray points represent HI 21 cm non-detections below the intrinsic UV luminosity threshold of $10^{23} \text{ W Hz}^{-1}$ and black open symbols represent sources with an UV luminosity above the threshold. The solid red symbols represent 21 cm detections. The shape of the symbols represent the radio source identification: circles represent GPS, CSS, and CSO sources and triangles represent FSRSs. The horizontal dotted line indicates the threshold for damped Ly α systems

Foundation. Parts of this research were supported by the Australian Research Council Centre of Excellence for All Sky Astrophysics in 3 Dimensions (ASTRO 3D), through project number CE170100013. The authors acknowledge the invaluable labor of the maintenance and clerical staff at their institutions, whose contributions make scientific discoveries a reality. KG acknowledges the staff at the University House for the supportive and collaborative writing environment.

Facilities: GBT

Software: GBTIDL (Marganian et al. 2006)

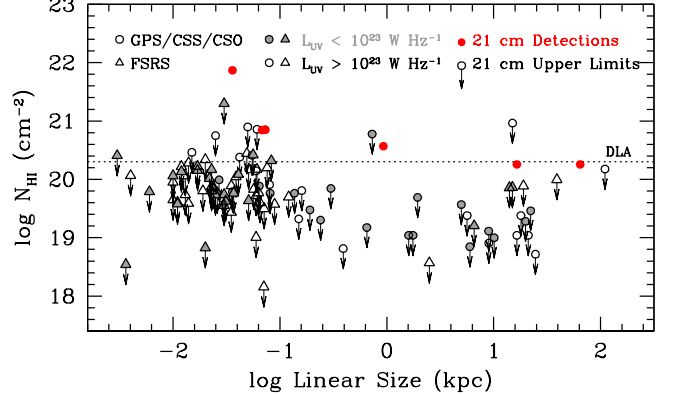


Figure 11. HI column density (upper limit for sources not detected in HI) versus linear size of the radio source. The solid red symbols represent 21 cm detections, the filled gray data points represent non-detections with an intrinsic UV luminosity below the UV threshold, and black open symbols represent non-detections with a UV luminosity above the $10^{23} \text{ W Hz}^{-1}$ threshold. The shape of the symbols represent the radio source identification: circles represent GPS, CSS, and CSO sources and triangles represent FSRSs. The horizontal dotted line indicates the threshold for damped Ly α systems.

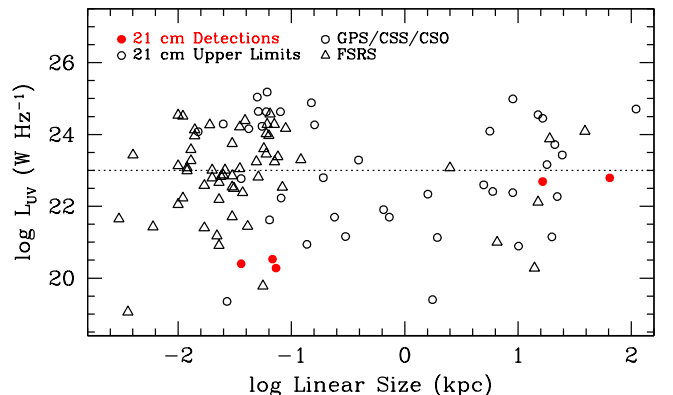


Figure 12. Ultraviolet luminosity versus linear size of the radio sources. The solid red symbols represent 21 cm detections and black symbols represent the upper limits to the column density for non-detections. The shape of the symbols represent the radio source identification: circles representing GPS, CSS, and CSO sources and triangles represent FSRSs. The horizontal dotted line indicates the UV luminosity threshold of ($L_{\text{UV}} > 10^{23} \text{ W Hz}^{-1}$).

REFERENCES

- Adelman-McCarthy, J. K., Agüeros, M. A., Allam, S. S. et al. 2008, ApJS, 175, 297
- Aditya, J. N. H. S., Kanekar, N., & Kurapati, S. 2016, MNRAS, 455, 5000
- Aditya, J. N. H. S., Kanekar, N., Prochaska, J. X., et al. 2017, MNRAS, 465, 5011
- Aditya, J. N. H. S. & Kanekar, N. 2018a, MNRAS, 473, 59
- Aditya, J. N. H. S. & Kanekar, N. 2018b, MNRAS, 481, 1578
- Allen, D. A., Ward, M. J., & Hyland, A. R. 1982, MNRAS, 199, 969
- Antonucci, R. R. J., & Ulvestad, J. S. 1985, ApJ, 294, 158
- Atlee, D. W. & Gould, A. 2007, ApJ, 664, 53
- Augusto, P., Gonzalez-Serrano, J. I., Perez-Fournon, I., & Wilkinson, P. N. 2006, MNRAS, 368, 1411
- Bajtlik, S., Duncan, R. C., Ostriker, J. P., 1988, ApJ, 327, 570
- Bessell, M. S. 1979, PASP, 91, 589
- Camps, H., Rieke, G. H., & Lebofsky, M. J. 1985, AJ, 90, 896
- Carballo, R., González-Serrano, J. I., Benn, C. R., Sánchez, S. F., & Vigotti, M. 1999, MNRAS, 306, 137

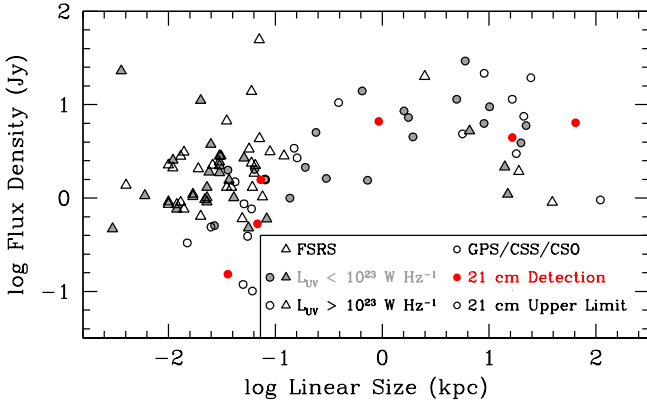


Figure 13. Continuum flux density (Jy) as a function of the linear size of the radio emission structures in the sample. The solid red symbols represent 21 cm detections and unfilled black symbols represent non-detections. The shape of the symbols indicates the radio source identification: circles represent GPS, CSS, and CSO sources and triangles represent FSRSs.

- Carilli, C. L., Menten, K. M., Reid, M. J., Rupen, M. P., & Yun, M. S. 1998, ApJ, 498, 175
 Chen, P. S., Fu, H. W., & Gao, Y. F. 2005, NewA, 11, 27
 Chengalur, J. N., de Bruyn, A. G., & Narasimha, D. 1999, ASPC, 156, 228
 Chengalur, J. N. & Kanekar, N. 2003, Phys. Rev. Lett., 91, 241302
 Chun, M. R., Gharanfali, S., Kulkarni, V. P., & Takamiya, M. 2006, AJ, 131, 686
 Cody, A. M. & Braun, R. 2009, A&A, 400, 871
 Condon, J. J., Hicks, P. D., & Jauncey, D. L. 1977, AJ, 82, 692
 Condon, J. J., Cotton, W. D., Greisen, E. W., & Yin, Q. F. 1998, AJ, 115, 1693
 Cowie, L. L. & Songaila, A. 1995, ApJ, 453, 596
 Curran, S. J., Whiting, M. T., Murphy, M. T. 2006, MNRAS, 371, 431
 Curran, S. J., Whiting, M. T., Wiklind, T., Webb, J. K., Murphy, M. T., & Purcell, C. R. 2008, MNRAS, 391, 765
 Curran, S. J. & Whiting, M. T. 2010, ApJ, 712, 303
 Curran, S. J. 2010, MNRAS, 402, 2647
 Curran, S. J., Whiting, M. T., Murphy, M. T., et al. 2011, MNRAS, 413, 1165
 Curran, S. J., Whiting, M. T., Sadler, E. M., & Bignell, C. 2013, MNRAS, 428, 2053
 Curran, S. J., Duchesne, S. W., Divoli, A., & Allison, J. R. 2016, MNRAS, 462, 4197
 Curran, S. J., Hunstead, R. W., Johnston, H. M., et al. 2017, MNRAS, 470, 4600
 Curran, S. J. 2018, PASA, 35, 36
 Curran, S. J., Hunstead, R. W., Johnston, H. M., et al. 2019, MNRAS, 484, 1182
 Darling, J. 2003, Phys. Rev. Lett., 91, 011301
 Darling, J. 2004, ApJ, 612, 58
 de Vries, W. H., Barthel, P. D., & O'Dea, C. P. 1997, A&A, 321, 105
 de Vries, W. H., O'Dea, C. P., Baum, S. A., et al. 1997b, ApJS, 110, 191
 de Vries, W. H., O'Dea, C. P., Perlman, E., Baum, S. A., Lehnert, M. D., Stocke, J., Rector, T., & Elston, R. 1998, ApJ, 503, 138
 de Vries, W. H., O'Dea, C. P., Barthel, P. D., et al. 2000, ApJ, 120, 2300
 Douglas, J. N., Bash, F. N., & Bozian, F. A. 1996, AJ, 111, 1954
 Drake, C. L., McGregor, P. J., & Dopita, M. A. 2004, AJ, 128, 955
 Drinkwater, M. J., Webster, R. L., Francis, P. J., et al. 1997, MNRAS, 284, 85
 Elitzur, M. 1992, Astronomical Masers (Dordrecht: Kluwer); <http://adsabs.harvard.edu/abs/1992ASSL..170....E>
 Ellison, S. L., Hall, P. B., & Lira, P. 2005, AJ, 130, 1345
 Elvis, M., Wilkes, B. J., McDowell, J. C., et al. 1994, ApJS, 95, 1
 Fanti, C., Fanti, R., Parma, P., et al. 1989, A&A, 217, 44
 Fanti, R., Fanti, C., Schilizzi, R. T., et al. 1990, A&A, 231, 333
 Fanti, C., Pozzi, F., Dallacasa, D., et al. 2001, A&A, 369, 380

- Fey, A. L. & Charlot, P. 1997, ApJS, 111, 95
 Fey, A. L. & Charlot, P. 2000, ApJS, 128, 17
 Ficarra, A., Grueff, G., & Tomassetti, G. 1985, A&AS, 59, 255
 Field, G. B. 1959, ApJ, 129, 536
 Fiorucci, M., Ciprini, S., & Tosti, G. 2004, A&A, 419, 25
 Fomalont, E. B., Frey, S., Paragi, Z., et al. 2000, ApJS, 131, 95
 Francis, P. J., Whiting, M. T., & Webster, R. L. 2000, PASP, 112, 56
 Fugmann, W. 1988, A&A, 205, 86
 Gardner, F. F. & Whiteoak, J. B. 1978, MNRAS, 183, 711
 Gelderman, R. & Whittle, M. 1994, ApJS, 91, 491
 Geréb, K., Morganti, R., & Oosterloo, T. A. 2014, A&A, 569, A35
 Geréb, K., Maccagni, F. M., Morganti, R., & Oosterloo, T. A. 2015, A&A, 575, 44
 Glass, I. S. 1981, MNRAS, 194, 795
 Godwin, J. G., Bucknell, M. J., Dixon, K. L., Green, M. R., Peach, J. V., & Wallis, R. E. 1977, Obs, 97, 238
 Gupta, N., Salter, C. J., Saikia, D. J., Ghosh, T., & Jeyakumar, S. 2006, MNRAS, 373, 972
 Gurvits, L. I., Kellermann, K. I., & Frey, S. 1999, A&A, 342, 378
 Hamby, N., MacGillivray, H. T., Read, M. A., et al. 2001, MNRAS, 326, 1279
 Healey, S. E., Romani, R. W., Taylor, G. B., et al. 2007, ApJS, 171, 61
 Healey, S. E., Romani, R. W., Cotter, G., et al. 2008, ApJS, 175, 97
 Hyland, A. R. & Allen, D. A. 1982, MNRAS, 199, 943
 Ishwara-Chandra, C. H., Dwarakanath, K. S. & Anantharamaiah, K. R. 2003, JA&A, 24, 37
 Jackson, C. A., Wall, J. V., Shaver, P. A., Kellermann, K. I., Hook, I. M., & Hawkins, M. R. S. 2002, A&A, 386, 97
 Jones, T. W., O'Dell, S. L., & Stein, W. A. 1974, ApJ, 192, 261
 Jorgenson, R. A., Wolfe, A. M., Prochaska, J. X., et al. 2006, ApJ, 646, 730
 Kanekar, N., Chengalur, J. N., de Bruyn, A. G., & Narasimha, D. 2003, MNRAS, 345, 7
 Kanekar, N. & Chengalur, J. N. 2003, A&A, 399, 857
 Kanekar, N. & Chengalur, J. N. 2004, MNRAS, 350, 17
 Kanekar, N., Carilli, C. L., Langston, G. I., et al. 2005, Phys. Rev. Lett., 95, 261301
 Kanekar, N., Subrahmanyam, R., Ellison, S. L., et al. 2006, MNRAS, 370, L46
 Kanekar, N., Langston, G. I., Stocke, J. T., Carilli, C. L. & Menten, K. M. 2012, ApJ, 746, L16
 Kanekar, N., Prochaska, J. X., Smette, A., et al. 2014, MNRAS, 438, 2131
 Kanekar, N., Ghosh, T., & Chengalur, J. N. 2018, Phys. Rev. Lett., 120, 061302
 Kellermann, K. I., Vermeulen, R. C., Zensus, J. A., & Cohen, M. H. 1998, AJ, 115, 1295
 Komatsu, E., Smith, K. M., Dunkley, J., et al. 2011, ApJS, 192, 18
 Kotilainen, J. K., Hyvönen, T., & Falomo, R. 2005, A&A, 440, 831
 Kuhn, O. P. 2004, MNRAS, 348, 647
 Labiano, A., Barthel, P. D., O'Dea, C. P., de Vries, W. H., Pérez, I., & Baum, S. A. 2007, A&A, 463, 97
 Laing, R. A. & Peacock, J. A. 1980, MNRAS, 190, 903
 Large, M. I., Mills, B. Y., Little, A. G., Crawford, D. F., & Sutton, J. M. 1981, MNRAS, 194, 693
 Lister, M. L. & Homan, D. C. 2005, AJ, 130, 1389
 Maccagni, F. M., Morganti, R., Oosterloo, T. A., Geréb, K., & Maddox, N. 2017, A&A, 604, A43
 Marganian, P., Garwood, R. W., Braatz, J. A., Radziwill, N. M., & Maddalena, R. J. 2006, ASPC, 351, 512
 Matthews, T. A. & Sandage, A. R. 1963, ApJ, 138, 30
 McAlary, C. W., McLaren, R. A., McGonegal, R. J. & Maza, J. 1983, ApJS, 52, 341
 Menon, T. K. 1983, AJ, 88, 598
 Molina, M., Landi, R., Bassini, et al. 2012, A&A, 548, 32
 Moore, C. B., Carilli, C. L., & Menten, K. M. 1999, ApJ, 510, L87
 Morganti, R., Killeen, N. E. B., & Tadhunter, C. N., 1993, MNRAS, 263, 1023
 Morganti, R., Oosterloo, T. A., Reynolds, J. E., & Tadhunter, C. N. 1997, MNRAS, 284, 541
 Morganti, R., Oosterloo, T. A., Tadhunter, C. N., van Moorsel, G., Killeen, N., & Wills, K. A. 2001, MNRAS, 323, 331

- Moss, V. A., Allison, J. R., Sadler, E. M., et al. 2017, MNRAS, 471, 2952
- Murphy, D. W., Browne, I. W. A., & Perley, R. A. 1993, MNRAS, 264, 298
- Murphy, M. T., Webb, J. K., Flambaum, V. V., et al. 2001, MNRAS, 327, 1208
- O'Dea, C. P., Baum, S. A., & Stanghellini, C. 1991, ApJ, 380, 660
- O'Dea, C. P. & Baum, S. A. 1997, ApJ, 113, 148
- O'Dell, S. L., Puschell, J. J., Stein, W. A., & Warner, J. W. 1978, ApJS, 38, 267
- Odell, S. L., Puschell, J. J., Stein, W. A., et al. 1978a, ApJ, 224, 22
- Ojha, R., Zacharias, N., Hennessy, G. S., Gaume, R. A., & Johnston, K. J. 2009, AJ, 138, 845
- Orienti, M., Dallacasa, D., & Stanghellini, C. 2007, A&A, 475, 813
- Owsianki, I. & Conway, J. E. 1998, A&A, 337, 69
- Peacock, J. A. & Wall, J. V. 1982, MNRAS, 198, 843
- Peck, A. B. & Taylor, G. B. 2000, ApJ, 534, 90
- Petrov, L., Kovalev, Y. Y., Fomalont, E. B., & Gordon, D. 2008, AJ, 136, 580
- Pihlström, Y. M., Conway, J. E., & Vermeulen, R. C. 2003, A&A, 404, 871
- Rahmani, H., Srianand, R., Gupta, N., et al. 2012, MNRAS, 425, 556
- Ramírez, A., de Diego, J. A., Dultzin-Hacyan, D., & González-Pérez, J. N. 2004, A&A, 421, 83
- Rao, S. A., Turnshek, D. A., & Nestor, D. B. 2006, ApJ, 636, 610
- Readhead, A. C. S., Taylor, G. B., Xu, W., Pearson, T. J., Wilkinson, P. N., & Polatidis, A. G. 1996, ApJ, 460, 612
- Rengelink, R. B., Tang, Y., de Bruyn, A. G., et al. 1997, A&A, 124, 259
- Rhee, J., Lah, P., Briggs, F. H., et al. 2018, MNRAS, 473, 1879
- Roberts, M. S. 1970, ApJ, 161, L9
- Sandage, A. 1965, ApJ, 141, 1560
- Sandage, A., Philippe, V., & Wyndham, J. D. 1965a, ApJ, 142, 1307
- Sandage, A. & Wyndham, J. D. 1965b, ApJ, 141, 328
- Sbarufatti, B., Treves, A., Falomo, R., Heidt, J., Kotilainen, J., & Scarpa, R. 2005, AJ, 129, 559
- Sbarufatti, B., Ciprini, S., Kotilainen, J., et al. 2009, AJ, 137, 337
- Schmitt, H. R. & Kinney, A. L. 1996, ApJ, 463, 498
- Schneider, D. P., Gunn, J. E., & Hoessel, J. G. 1983, ApJ, 264, 337
- Shen, Z. -Q., Wan, T. -S., Moran, J. M., Jauncey, D. L., Reynolds, J. E., & Tzioumis, A. K. 1997, AJ, 114, 1999
- Shen, Z. -Q., Wan, T. -S., Moran, J. M., et al. 1998, AJ, 115, 1357
- Simpson, C. & Rawlings, S. 2000, MNRAS, 317, 1023
- Skrutskie, M. F., Cutri, R. M., Stiening, R., et al. 2006, AJ, 131, 1163
- Smith, E. P. & Heckman, T. M. 1989, ApJS, 69, 365
- Smith, J. A., Tucker, D. L., Kent, S., et al. 2002, AJ, 123, 2121
- Snellen, A. G., Lehnert, M. D., Bremer, M. N., & Schilizzi, R. T. 2002, MNRAS, 337, 981
- Spencer, R. E., McDowell, J. C., Charlesworth, M., Fanti, C., Parma, P., & Peacock, J. A. 1989, MNRAS, 240, 657
- Srianand, R., Gupta, N., Petitjean, P., Noterdaeme, P., & Ledoux, C. 2010, MNRAS, 405, 1888
- Stanghellini, C., Baum, S. A., O'Dea, C. P., & Morris, G. B. 1990, A&A, 233, 379
- Stanghellini, C., O'Dea, C. P., Baum, S. A., & Laurikainen, E. 1993, ApJS, 88, 1
- Stanghellini, C., O'Dea, C. P., Dallacasa, D., Baum, S. A., Fanti, R., & Fanti, C. 1998, A&AS, 131, 303
- Stanghellini, C., O'Dea, C. P., Dallacasa, D., et al. 2005, A&A, 443, 891
- Stickel, M. & Kuehr, H. 1996, A&AS, 115, 11
- Tapia, S., Craine, E. R., & Johnson, K. 1976, ApJ, 203, 291
- Tzanavaris, P., Webb, J. T., Murphy, M. T., Flambaum, V. V., & Curran, S. J. 2005, Phys. Rev. Lett., 95, 041301
- Tzanavaris, P., Murphy, M. T., Webb, J. T., Flambaum, V. V., & Curran, S. J. 2007, MNRAS, 374, 634
- Uson, J. M., Bagri, D. S., & Cornwell, T. J. 1991, Phys. Rev. Lett., 67, 3328
- van Gorkom, J. H., Knapp, G. R., Ekers, R. D., Ekers, D. D., Laing, R. A., & Polk, K. S. 1989, AJ, 97, 708
- van Langevelde, H. J., van Dishoeck, E. F., Sevenster, M. N., & Israel, F. P. 1995, ApJ, 448, L123
- Vermeulen, R. C., Pihlström, Y. M., Tschager, W., et al. 2003, A&A, 404, 861
- White, R. L. & Becker, R. H. 1992, ApJS, 79, 331
- Wilkinson, P. N., Polatidis, A. G., Readhead, A. C. S., Xu, W., & Pearson, T. J. 1994, ApJ, 432, L87
- Wills, D. & Lynds, R. 1978, ApJS, 36, 317
- Wolfe, A. M. & Burbidge, G. R. 1975, ApJ, 200, 548
- Wright, A. E., Ables, J. G., & Allen, D. A. 1983, MNRAS, 205, 793
- Wright, E. L. 2006, PASP, 118, 117
- Xiang, L., Dallacasa, D., Cassaro, P., Jiang, D., & Reynolds, C. 2005, A&A, 434, 123
- Xu, W., Readhead, A. C. S., Pearson, T. J., Polatidis, A. G., & Wilkinson, P. N. 1995, ApJS, 99, 297
- Yan, T., Stocke, J. T., Darling, J., & Hearty, F. 2012, AJ, 144, 124
- Yan, T., Stocke, J. T., Darling, J., Momjian, E., Sharma, S., & Kanekar, N. 2016, AJ, 151, 74

Table 1
Observations of Intrinsic HI and OH Lines Toward Compact Radio Sources

Source	α (J2000)	δ (J2000)	z	ν_{HI} (MHz)	HI Time (sec)	OH Time (sec)	Class.	References
							Class.	Spec.
0018+729	00 21 27.4	+73 12 41.9	0.821(2)	780.0(9)	1493	896	GPS	1
LBQS 0106+0119	01 08 38.8	+01 35 00.3	2.099(5)	472.1(8)	564	541	FSRS	2
COINS J0111+3906	01 11 37.3	+39 06 28.1	0.66847(3)	851.322(15)	1800	...	GPS,CSO	1,3,4
UM321	01 25 28.8	-00 05 55.9	1.07481(15)	684.60(5)	298	265	FSRS	2
3C43	01 29 59.8	+23 38 20.3	1.459	577.6	1773	1725	CSS	3,5,6,7
0133+476	01 36 58.6	+47 51 29.1	0.859	764.1	293	290	FSRS	2,8
3C48	01 37 41.3	+33 09 35.1	0.367	1038	378	366	CSS	3,5,6
3C49	01 41 09.2	+13 53 28.1	0.62	876.8	893	...	CSS	3,5,6,7
0138-097	01 41 25.8	-09 28 43.7	0.733	818.6	298	271	FSRS	2
PKS 0201+113	02 03 46.7	+11 34 45.4	3.6390(10)	306.19(7)	2377	2377	GPS	1
0212+735	02 17 30.8	+73 49 32.6	2.367	421.9	528	502	FSRS	2,8
B2 0218+357	02 21 05.5	+35 56 13.7	0.944(2)	730.7(8)	270	264	FSRS	2
3C066A	02 22 39.6	+43 02 07.8	0.444	982.7	299	286	FSRS	8
0221+067	02 24 28.4	+06 59 23.3	0.511	940.0	296	272	FSRS	2,8
4C+34.07	02 26 10.3	+34 21 30.3	2.910(2)	363.28(19)	2388	1763	CSS	3,5,6
HB89 0235+164	02 38 38.9	+16 36 59.3	0.940	732.2	281	273	FSRS	2,8
PKS 0237-23	02 40 08.2	-23 09 15.8	2.223	440.71	1493	3284	GPS	1,3
PKS 0239+108	02 42 29.2	+11 01 00.7	2.694	384.5	322	309	FSRS	2
B3 0248+430	02 51 34.5	+43 15 15.8	1.31	614.9	1493	...	GPS	1,3
0306+102	03 09 03.6	+10 29 16.3	0.863	761.4	297	256	FSRS	2,8
NGC 1275	03 19 48.2	+41 30 42.1	0.01765(4)	1395.77(5)	278	...	FSRS	2,8

Table 1 — *Continued*

Source	α (J2000)	δ (J2000)	z	ν_{HI} (MHz)	HI Time (sec)	OH Time (sec)	Class.	References
							Class.	Spec.
OE+131	03 21 52.1	+12 21 14.0	2.662	387.88	1472	1790	GPS,CSS	3,5,6,7
PKS 0327–241	03 29 54.1	−23 57 08.8	0.895	748.6	278	285	FSRS	2
0336–019	03 39 30.9	−01 46 35.8	0.852	767.0	290	288	FSRS	2
0346–279	03 48 38.1	−27 49 13.6	0.991	712.4	297	263	FSRS	2
4C+76.03	04 10 45.6	+76 56 45.3	0.5985	888.6	818	896	GPS,CSS	3,5,6,7
0420–014	04 23 15.8	−01 20 33.1	0.91609(18)	741.30(7)	278	297	FSRS	2
0422+004	04 24 46.8	+00 36 06.3	0.310	1084.3	266	288	FSRS	2,8
3C119	04 32 36.5	+41 38 28.4	1.023	702.1	1790	1791	CSS	3,5,6,7
0440–003	04 42 38.7	−00 17 43.4	0.844	769.3	274	289	FSRS	2
PKS 0454–234	04 57 03.2	−23 24 52.0	1.003	708.1	298	266	FSRS	2
PKS 0457+024	04 59 52.1	+02 29 31.2	2.384	419.7	1791	1721	GPS	1,3
0458–020	05 01 12.8	−01 59 14.3	2.286	432.3	680	621	FSRS	2,8
PKS 0500+019	05 03 21.2	+02 03 04.7	0.58457(2)	896.398(11)	164	...	GPS	1,3
3C138	05 21 09.9	+16 38 22.1	0.76	807.1	550	1790	CSS	3,5,6
PKS 0528–250	05 30 08.0	−25 03 29.9	2.813	372.5	2651	1493	GPS	1
PKS 0539–057	05 41 38.1	−05 41 49.4	0.839(3)	772.4(1.3)	298	250	FSRS	2
3C147	05 42 36.1	+49 51 07.2	0.55	916.39	250	1791	CSS	3,5,6
B3 0552+398	05 55 30.8	+39 48 49.2	2.365(5)	422.1(6)	1767	288	GPS	1
0605–085	06 07 59.7	−08 34 50.0	0.872	757.8	516	489	FSRS	2
0607–157	06 09 41.0	−15 42 40.7	0.3240(10)	1072.8(8)	263	149	FSRS	2
HB89 0636+680	06 42 04.3	+67 58 35.6	3.1800(10)	339.81(8)	1941	896	GPS	1
B2 0711+35	07 14 42.8	+35 34 39.8	1.62	542.1	2302	2293	GPS	1
0735+178	07 38 07.4	+17 42 19.0	0.424	996.5	298	381	FSRS	2,8
0736+017	07 39 18.0	+01 37 04.6	0.189410(9)	1192	349	321	FSRS	2,8
B2 0738+31	07 41 10.7	+31 12 00.2	0.6314(16)	870.7(9)	1194	1742	GPS	1,3
PKS 0742+10	07 45 33.1	+10 11 12.7	2.624(3)	391.9(3)	1681	1681	GPS	1,3
PKS 0743–006	07 45 54.1	−00 44 17.5	0.994	712.3	278	1182	GPS	1,3
3C186	07 44 17.5	+37 53 17.2	1.0670(19)	687.2(6)	1790	1790	CSS	3,5,6
PKS 0745+241	07 48 36.1	+24 00 24.1	0.4092(10)	1008.0(7)	271	245	FSRS	2,8
0748+126	07 50 52.0	+12 31 04.8	0.889	750.9	283	297	FSRS	8,9
COINS J0753+4231	07 53 03.3	+42 31 30.8	3.5892(8)	309.51(5)	2687	2687	CSO	4
HB89 0754+100	07 57 06.6	+09 56 34.9	0.2660(10)	1122.0(9)	232	390	FSRS	2,8
3C190	08 01 33.5	+14 14 42.4	1.1944(12)	647.3(4)	528	...	CSS	3,5,6
SBS 0804+499	08 08 39.7	+49 50 36.5	1.430(2)	584.5(5)	596	592	FSRS	2
PKS 0823+033	08 25 50.3	+03 09 24.5	0.506	942.2	262	285	FSRS	8,8
PKS 0823–223	08 26 01.6	−22 30 27.2	0.910	742.7	298	283	FSRS	9
0828+493	08 32 23.2	+49 13 21.0	0.548	916.6	256	292	FSRS	2
0836+710	08 41 24.7	+70 53 42.2	2.1720(10)	447.80(14)	291	260	FSRS	2,8
OJ+287	08 54 48.9	+20 06 30.6	0.306	1087.6	270	...	FSRS	2,8
PKS 0858–279	09 00 40.0	−28 08 20.3	2.152	450.6	400	...	GPS	1
TXS 0902+490	09 05 27.5	+48 50 50.0	2.6887(11)	385.07(11)	1433	1493	GPS	1
0906+015	09 09 10.1	+01 21 35.6	1.020(3)	701.8(1.1)	290	285	FSRS	2,8
3C216	09 09 33.5	+42 53 46.5	0.6703(12)	850.4(6)	1492	3581	CSS	5,6
0917+449	09 20 58.5	+44 41 54.0	2.1899(2)	445.28(3)	577	369	FSRS	2,8
0919–260	09 21 29.4	−26 18 43.4	2.300	429.4	597	592	FSRS	2
0923+392	09 27 03.0	+39 02 20.9	0.6952(3)	837.90(15)	298	274	FSRS	2
0925–203	09 27 51.8	−20 34 51.2	0.34741(15)	1053.71(2)	298	526	FSRS	2
HB89 0954+556	09 57 38.2	+55 22 57.8	0.896(8)	749(3)	268	284	FSRS	2
HB89 0954+658	09 58 47.2	+65 33 54.8	0.368	1037	292	...	FSRS	2
1004+141	10 07 41.5	+13 56 29.6	2.707(5)	383.2(5)	519	517	FSRS	2,8
3C237	10 08 00.0	+07 30 16.4	0.87	759.6	1785	1771	CSS	3,5,6
PKS 1034–293	10 37 16.1	−29 34 02.8	0.312	1082	582	562	FSRS	2
1055+018	10 58 29.6	+01 33 58.8	0.888(5)	752(2)	243	266	FSRS	2,8
1116+128	11 18 57.3	+12 34 41.7	2.129(2)	454.0(3)	567	542	FSRS	2,8
PKS 1124–186	11 27 04.4	−18 57 17.4	1.050	691.9	249	289	FSRS	2,9
B3 1144+402	11 46 58.3	+39 58 34.3	1.0880(10)	680.3(3)	262	296	FSRS	2,8
FBQs J1159+2914	11 59 31.8	+29 14 43.8	0.7245(11)	823.7(5)	298	291	FSRS	2,8
1202–262	12 05 33.2	−26 34 04.5	0.789	794.0	291	286	FSRS	2
B2 1219+28	12 21 31.7	+28 13 58.5	0.102	1288	596	...	FSRS	2
1222+037	12 24 52.4	+03 30 50.3	0.9556(11)	726.3(4)	261	290	FSRS	2,8
PG 1222+216	12 24 54.5	+21 22 46.4	0.4320(10)	991.9(7)	299	273	FSRS	2,8
B2 1225+36	12 27 58.7	+36 35 11.8	1.973(2)	477.8(3)	300	...	GPS,CSS	1,3,5,6
3C273	12 29 06.7	+02 03 08.6	0.15834(7)	1226.24(7)	595	562	FSRS	2,8
COINS J1244+4048	12 44 49.2	+40 48 06.2	0.813(2)	783.5(9)	442	2239	CSO	4
3C279	12 56 11.2	−05 47 21.5	0.5362(14)	924.6(2)	269	275	FSRS	2
1308+326	13 10 28.7	+32 20 43.8	0.996	711.6	228	298	FSRS	2,8
3C287	13 30 37.7	+25 09 10.9	1.055	691.2	1790	1770	CSS	3,5,6
3C286	13 31 08.3	+30 30 33.0	0.8494(11)	768.0(5)	1194	1194	CSS	3,5,6
HB89 1333+459	13 35 22.0	+45 42 38.2	2.4490(10)	411.83(12)	1750	...	GPS	1
1354+195	13 57 04.4	+19 19 07.4	0.720	824.8	274	...	FSRS	2,8
B3 1355+441	13 57 40.6	+43 53 59.8	0.646	862.9	844	1762	GPS,CSO	1,4
1418+546	14 19 46.6	+54 23 14.8	0.1526(3)	1232.4(3)	272	275	FSRS	2,8
3C305.1	14 47 09.6	+76 56 21.8	1.132	666.2	895	...	CSS	3,5,6
3C309.1	14 59 07.6	+71 40 19.9	0.905	745.6	896	865	CSS	3,5,6
1504–166	15 07 04.8	−16 52 30.3	0.876(4)	757.2(1.6)	281	...	FSRS	2

Table 1 — *Continued*

Source	α (J2000)	δ (J2000)	z	ν_{HI} (MHz)	HI Time (sec)	OH Time (sec)	Class.	References Class.	References Spec.
3C318	15 20 05.4	+20 16 05.8	1.5740(10)	551.8(2)	448	896	CSS	3,5,6	
COINS J1546+0026	15 46 09.5	+00 26 24.6	0.55	916.4	1782	1777	GPS,CSO	4	2
B2 1600+33	16 02 07.3	+33 26 53.1	1.1	676.4	862	...	GPS,CSS	1,3,5,6	
PKS 1622–253	16 25 46.9	−25 27 38.3	0.786	794.3	277	291	FSRS	2	
PKS 1622–29	16 26 06.0	−29 51 27.0	0.815	781.6	266	298	FSRS	11	
3C343	16 34 33.8	+62 45 35.8	0.988	714.5	1194	1197	CSS	3,5,6,7	
1637+574	16 38 13.5	+57 20 24.0	0.7506(10)	811.4(5)	265	214	FSRS	2,8	
3C343.1	16 38 28.2	+62 34 44.3	0.75	811.7	1800	1787	CSS	3,5,6,7	
1642+690	16 44 07.9	+68 56 39.8	0.751	810.2	290	261	FSRS	2,8	2
1656+053	16 58 33.5	+05 15 16.4	0.879	754.9	282	261	FSRS	2,8	
1730–130	17 33 02.7	−13 04 49.5	0.902	745.8	284	280	FSRS	2	
1741–038	17 43 58.9	−03 50 04.6	1.054	691.5	271	298	FSRS	2	
1749+701	17 48 32.8	+70 05 50.8	0.770	801.5	278	278	FSRS	2,8	
1803+784	18 00 45.7	+78 28 04.0	0.680	844.5	298	...	FSRS	2,8	
1800+440	18 01 32.3	+44 04 21.9	0.663	845.1	288	...	FSRS	2,8	
COINS J1815+6127	18 15 36.8	+61 27 11.6	0.601(3)	887.2(1.7)	1436	2090	GPS,CSO	4	2
1823+568	18 24 07.1	+56 51 01.5	0.6640(10)	853.6(5)	288	260	FSRS	2	
3C380	18 29 31.8	+48 44 16.2	0.69	840.5	597	384	CSS	5,6	2
4C+29.56	18 31 14.9	+29 07 10.3	0.842(3)	771.1(1.3)	1293	1493	CSS	3,5,6	2
WMAP 1849+6705	18 49 16.1	+67 05 41.7	0.6570(10)	857.2(5)	283	296	FSRS	2,8	
TXS 1848+283	18 50 27.6	+28 25 13.2	2.56	398.9	1791	3583	GPS	1	
TXS 1851+488	18 52 28.5	+48 55 47.5	1.250(3)	631.3(8)	597	...	GPS	1	
1921–293	19 24 51.1	−29 14 30.1	0.35263(18)	1050.11(14)	381	...	FSRS	2	
PKS 2000–330	20 03 24.1	−32 51 45.1	3.7730(10)	297.59(6)	1720	1744	GPS	1	
2007+777	20 05 30.9	+77 52 43.1	0.342	1058.4	394	...	FSRS	2,8	
PKS 2008–068	20 11 12.2	−06 44 03.6	0.5470(10)	918.2(6)	1740	1791	GPS	1,3,7	
COINS J2022+6136	20 22 09.7	+61 36 58.8	0.227	1157	258	285	GPS	12	2
2059+034	21 01 38.8	+03 41 31.3	1.013	705.6	242	290	FSRS	2	
PKS 2121–01	21 23 39.1	−01 12 34.7	1.158(2)	658.2(6)	299	...	GPS,CSO	1,10	
PKS 2126–15	21 29 12.2	−15 38 41.0	3.2680(10)	332.80(8)	3583	3583	GPS	1,3	
PKS 2127+04	21 30 32.9	+05 02 17.5	0.99	713.8	893	896	GPS	1,3	
2128–123	21 31 35.3	−12 07 04.8	0.501	945.3	384	366	FSRS	2	
PKS 2134+004	21 36 38.6	+00 41 54.2	1.9320(10)	484.45(17)	1791	...	GPS	3	
PKS 2135–209	21 37 50.0	−20 42 31.7	0.63634(3)	868.04(2)	...	1682	CSS	6	2
2145+067	21 48 05.5	+06 57 38.6	0.990	712.8	282	...	FSRS	2,8	
PKS 2149+056	21 51 37.9	+05 52 13.0	0.740(10)	816.3(5)	1790	...	GPS	1	1
2155–152	21 58 06.8	−15 01 09.3	0.672	848.5	278	386	FSRS	2	
2201+315	22 03 15.0	+31 45 38.3	0.2950(5)	1096.8(4)	398	280	FSRS	2,8	
2216–038	22 18 52.0	−03 35 36.9	0.901	746.2	281	255	FSRS	2	
PKS 2230+111	22 32 36.4	+11 43 50.9	1.037	697.3	1752	1791	CSS	5,6	
2234+282	22 36 22.5	+28 28 57.4	0.795	790.3	288	362	FSRS	2,8	
3C454.1	22 50 32.9	+71 29 19.2	1.841	499.97	896	...	CSS	3,5,6	
3C454	22 51 34.7	+18 48 40.1	1.757	515.2	1316	1752	CSS	3,5,6	
3C454.3	22 53 57.8	+16 08 53.6	0.859	763.1	252	266	FSRS	2,8	
3C455	22 55 03.9	+13 13 34.0	0.543	920.6	1790	1791	CSS	3,5,6	2
2255–282	22 58 06.0	−27 58 21.3	0.92584(15)	737.69(6)	273	296	FSRS	2	
3C459	23 16 35.2	+04 05 18.1	0.22012(3)	1164.15(3)	292	286	CSS	13	
HB89 2342+821	23 44 03.8	+82 26 40.4	0.735	818.7	1791	1752	GPS,CSS	1,3,5,6	2
HB89 2344+092	23 46 36.8	+09 30 45.5	0.677	847.0	298	263	FSRS	2,8	

Note. — Columns list the source name, Right Ascension and Declination, optical redshift, expected frequency of the corresponding HI 21 cm line, total integration times for each reduced spectra, radio source classification (GPS, CSS, CSO, FSRS), references for the classification, and references for any previous HI 21 cm observations. Numbers in parentheses indicate uncertainties in the final digit(s) of listed quantities, when available.

Classification references: 1 – de Vries, Barthel, & O’Dea (1997); 2 – Healey et al. (2007); 3 – O’Dea & Baum (1997); 4 – Peck & Taylor (2000); 5 – Fanti et al. (1990); 6 – Spencer et al. (1989); 7 – Morganti et al. (1997); 8 – Augusto et al. (2006); 9 – Condon et al. (1977); 10 – Xiang et al. (2005); 11 – Jackson et al. (2002); 12 – Fomalont et al. (2000); 13 – Gelderman & Whittle (1994).

Previous spectroscopy of the HI 21 cm line references: 1 – Carilli et al. (1998); 2 – Vermeulen et al. (2003); 3 – Gupta et al. (2006); 4 – Ishwara-Chandra et al. (2003); 5 – Curran et al. (2013).

Table 2 — HI 21 cm Line Observations, Column Densities, and Source Sizes

Source	z	ν (MHz)	Δv (km s ^{−1})	rms (mJy)	Ctnm (Jy)	N_{HI} (10^{20} cm ^{−2})	Prev. N_{HI}	Size (arcsec)	Size (kpc)	Ref.
0018+729	0.821(2)	780.0(9)	−5077, 6080	3.37	1.0033(6)	<0.51	...	0.018	0.14	1
LBQS 0106+0119	2.009(5)	472.1(8)	...	RFI	0.0106	0.09	2
COINS J0111+3906	0.66847(3)	853.322(15)	−1343, 3015	2.47	0.153(2)	74(13)	81(17) ¹	0.005	0.04	3
UM321	1.07481(15)	684.60(5)	−3813, 26560	8.3	1.306(18)	<1.1	...	0.0048	0.039	4
3C43	1.459	577.6	−3047, 2470	12.8	5.97(4)	<0.29	...	2.60	22.2	5
0133+476	0.859	764.1	...	RFI	0.0029	0.022	2
3C48	0.367	1038	−432, 568	4.9	20.04(4)	<0.037	...	0.50	2.5	5
3C49	0.62	876.8	...	RFI	1.1 ²	0.99	6.7	3

Table 2 — *Continued*

Source	z	ν (MHz)	Δv (km s $^{-1}$)	rms (mJy)	Ctnm (Jy)	N_{HI} (10^{20} cm $^{-2}$)	Prev. N_{HI}	Size (arcsec)	Ref. (kpc)
0138–097	0.733	818.6	–2423, 2711	9.9	0.76(12)	<1.9	...	0.0019	0.014
PKS 0201+113	3.6390(10)	306.19(7)	–2976, 10760	7.13	0.331(8)	<2.9	...	0.002	0.015
0212+735	2.367	421.9	...	RFI	0.0131	0.108
B2 0218+357	0.944(2)	730.7(8)	–1559, 4882	6.1	1.559(4)	<0.64	...	0.0052	0.037
3C066A	0.444	982.7	–3179, 2840	8.2	2.83(16)	<0.47	...	0.0053	0.030
0221+067	0.511	940.0	–462, 806	5.9	0.961(10)	<1.0	...	0.0035	0.022
4C+34.07	2.910(2)	363.28(19)	...	RFI	1.1	8.7
HB89 0235+164	0.940	732.2	–458, 1628	8.6	1.1(2)	<1.3	...	0.0021	0.017
PKS 0237–23	2.223	440.71	–327, 1721	4.10	3.42(2)	<0.21	...	0.018	0.15
PKS 0239+108	2.694	384.5	...	RFI	RFI ⁸	0.0024	0.019
B3 0248+430	1.31	614.9	...	RFI	< 0.78 ³	0.06	0.5
0306+102	0.863	761.4	–12690, 1262	8.0	0.47960(2)	<2.6	...	0.0073	0.056
NGC 1275	0.01765(4)	1395.77(5)	–2242, 2530	4.8	23(3)	<0.035	...	0.102	0.00361
OE+131	2.662	387.88	–8579, 10542	8.33	2.689(9)	<0.63	RFI ⁸	0.02	0.16
PKS 0327–241	0.895	748.6	–1668, 979	8.3	0.9197(4)	<1.5
0336–019	0.852	767.0	–3379, 3009	6.5	2.26(8)	<0.45	...	0.0013	0.010
0346–279	0.991	712.4	–1366, 418	9.7	1.03(6)	<1.6	...	0.0095	0.076
4C+76.03	0.5985	888.6	–391, 631	6.75	6.618(7)	3.7(1.1)	2.5 ²	0.14	0.93
0420–014	0.91609(18)	741.30(7)	...	RFI	0.0017	0.013
0422+004	0.310	1084.3	...	RFI	0.0029	0.013
3C119	1.023	702.1	–1221, 809	12.5	14.0(1.6)	<0.15	...	0.08	0.65
0440–003	0.844	769.3	–2391, 1888	8.1	2.37(4)	<0.53	...	0.0078	0.060
PKS 0454–234	1.003	708.1	...	RFI	0.0024	0.019
PKS 0457+024	2.384	419.7	–3714, 6678	5.23	0.390(19)	<2.6	...	0.0067	0.055
0458–020	2.286	432.3	...	RFI	0.0046	0.038
PKS 0500+019	0.58457(2)	896.398(11)	–1191, 314	7.13	1.57(7)	7.1(1.3)	7.0(1.3) ¹	0.011	0.073
3C138	0.76	807.1	–2775, 2039	7.76	11.42(4)	<0.10	< 0.10 ²	0.68	5.0
PKS 0528–250	2.813	372.5	–5883, 2197	5.95	1.6(3.6)	<0.81	...	0.010	0.080
PKS 0539–057	0.839(3)	772.4(1.3)	–1497, 2526	8.7	0.91(9)	<1.5	...	0.0030	0.023
3C147	0.55	916.4	–2522, 717	12	29.4(6)	<0.070	< 0.085 ²	0.94	6.0
B3 0552+398	2.365(5)	422.1(6)	–5078, 6761	4.83	0.490(7)	<1.9	...	0.003	0.03
0605–085	0.872	757.8	–2297, 1170	7.5	2.820(14)	<0.42	...	0.0040	0.031
0607–157	0.3240(10)	1072.8(8)	...	RFI	0.0146	0.068
HB89 0636+680	3.1800(10)	339.81(8)	–10896, 11619	7.24	0.119(2)	<7.9	...	0.006	0.05
B2 0711+35	1.62	542.1	–375, 4993	8.52	0.87(2)	<1.5	...	0.006	0.05
0735+178	0.424	996.5	–1511, 1569	4.6	2.16(4)	<0.34	...	2.6	14
0736+017	0.189410(9)	1194.21(2)	–1854, 2413	5.8	2.54(3)	<0.38	...	0.0036	0.011
B2 0738+31	0.6314(16)	870.7(9)	–840, 2672	19.2	1.491(6)	<2.4	< 0.45 ²	0.006	0.04
PKS 0742+10	2.624(3)	391.9(3)	–5033, 3071	5.24	1.562(6)	<0.58	< 1.4 ⁵	0.010	0.08
PKS 0743–006	0.994	712.3	...	RFI	0.005	0.04
3C186	1.0670(19)	687.2(6)	–1719, 2208	4.34	2.99(2)	<0.25	...	2.2	18
PKS 0745+241	0.4092(10)	1008.0(7)	–1890, 2257	4.8	1.038(9)	<0.73	...	0.0032	0.017
0748+126	0.889	750.9	...	RFI	0.0018	0.014
COINS J0753+4231	3.5892(8)	309.51(5)	–5318, 13086	8.32	0.7667(5)	<1.4	...	0.0086	0.06
HB89 0754+100	0.2660(10)	1122.0(9)	–491, 939	4.3	1.1(7)	<0.73	< 0.83 ⁹	3.7	15
3C190	1.1944(12)	647.3(4)	...	RFI	40 ⁴	4.1	34
SBS 0804+499	1.430(2)	584.5(5)	...	RFI	< 5.1 ¹⁰	0.0012	0.010
PKS 0823+033	0.506	942.2	–1880, 1825	5.7	1.3(6)	<0.76	...	0.0038	0.023
PKS 0823–223	0.910	742.7	–2907, 1540	8.6	0.64(6)	<2.2	...	0.0025	0.020
0828+493	0.548	916.6	–1150, 803	7.0	1.01(14)	<1.2	...	0.0064	0.041
0836+710	2.1720(10)	447.80(14)	...	RFI	0.0087	0.075
OJ+287	0.306	1087.6	...	RFI	0.0030	0.014
PKS 0858–279	2.152	450.6	–1924, 3340	13.9	0.86(1)	<2.9
TXS 0902+490	2.6887(11)	385.07(11)	–3636, 3916	6.94	0.954(4)	<1.5	< 7.2 ⁸	0.013	0.11
0906+015	1.020(3)	701.8(1.1)	...	RFI	0.0076	0.062
3C216	0.6703(12)	850.4(6)	–353, 3589	8.06	6.41(4)	1.8(4)	1.2 ²	9.2	64.5
0917+449	2.1899(2)	445.28(3)	...	RFI	0.0028	0.024
0919–260	2.300	429.4	–4715, 737	4.2	0.86(11)	<0.90	...	0.0012	0.010
0923+392	0.6952(3)	837.90(15)	–1669, 879	8.6	3.1(2)	<0.39	...	0.0020	0.014
0925–203	0.34741(15)	1053.71(2)	–1790, 1656	7.9	0.89(9)	<1.3
HB89 0954+556	0.896(8)	749(3)	–1837, 862	8.6	4.345(17)	<0.32	...	0.0089	0.071
HB89 0954+658	0.368	1037	–6182, 1058	6.8	0.7635(2)	<1.4	< 11 ⁶	0.0023	0.012
1004+141	2.707(5)	383.2(5)	–4512, 266	9.4	1.305(15)	<1.5	RFI ⁸	0.0074	0.061
3C237	0.87	759.6	–6394, 4732	6.29	9.47(6)	<0.10	...	1.3	10.1
PKS 1034–293	0.312	1082	–1129, 1975	4.4	1.06(11)	<0.62	...	0.013	0.006
1055+018	0.888(5)	752(2)	–3869, 2270	13	3.759(13)	<0.54	...	0.0032	0.025
1116+128	2.129(2)	454.0(3)	...	RFI	0.0094	0.081
PKS 1124–186	1.050	691.9	–2521, 1682	6.8	0.47(5)	<2.6	...	0.0004	0.003
B3 1144+402	1.0880(10)	680.3(3)	–1316, 2171	9.4	0.6038(4)	<2.8	...	0.0059	0.049
FBQS J1159+2914	0.7245(11)	823.7(5)	–7388, 8262	5.1	2.25(3)	<0.33	< 1.8 ²	0.036	0.026
1202–262	0.789	794.0	–640, 1326	5.3	2.2090(10)	<0.36	...	0.003	0.03
B2 1219+28	0.102	1288	–807, 1637	6.8	0.9(1.7)	<1.2	...	0.0072	0.013
1222+037	0.9556(11)	726.3(4)	–3436, 2880	8.5	0.85(9)	<1.7	...	0.0015	0.012

Table 2 — *Continued*

Source	z	ν (MHz)	Δv (km s $^{-1}$)	rms (mJy)	Ctnm (Jy)	N_{HI} (10 20 cm $^{-2}$)	Prev. N_{HI}	Size (arcsec)	Ref. (kpc)	
PG 1222+216	0.4320(10)	991.9(7)	-1988, 2095	8.2	2.06(9)	<0.64	...	0.0034	0.019	2
B2 1225+36	1.973(2)	477.8(3)	...	RFI	0.060	0.51	5
3C273	0.15834(7)	1226.24(7)	-9459, 2793	4.2	46.69(7)	<0.014	...	0.261	0.0706	2
COINS J1244+4048	0.813(2)	783.5(9)	-2334, 2138	7.5	1.62(3)	<0.70	...	0.04	0.3	12
3C279	0.5362(4)	924.6(2)	-1768, 3010	4.4	11.1(2)	<0.068	...	0.0032	0.020	2
1308+326	0.996	711.6	...	RFI	0.0038	0.031	2
3C287	1.055	691.2	-4133, 4190	4.03	10.5(3)	<0.066	...	0.048	0.39	5
3C286	0.8494(11)	768.0(5)	-3306, 3466	6.50	19.39(9)	<0.052	...	3.2	25	5
HB89 1333+459	2.4490(10)	411.83(12)	-8575, 6741	4.53	0.102(2)	<9.2	...	1.8	15	6
1354+195	0.720	824.8	-3694, 2424	8.2	3.13(7)	<0.38	...	0.0123	0.089	2
B3 1355+441	0.646	862.9	...	RFI	33 ²	0.017	0.12	3
1418+546	0.1526(3)	1232.4(3)	-3353, 4972	6.5	0.91(7)	<1.2	<2.7 ⁶	0.0038	0.010	2
3C305.1	1.132	666.2	...	RFI	2.34	19	5
3C309.1	0.905	745.6	-2810, 4021	7.89	11.457(5)	<0.11	...	2.11	16.5	5
1504-166	0.876(4)	757.2(1.6)	-5553, 3412	9.7	2.8(2)	<0.54	...	0.0017	0.0013	2
3C318	1.5740(10)	551.8(2)	-962, 869	5.89	6.3(2)	<0.13	...	1.05	8.98	5
COINS J1546+0026	0.55	916.4	-2895, 2676	2.99	2.027(11)	<0.25	< 0.25 ²	0.010	0.06	3
B2 1600+33	1.1	676.4	...	RFI	0.06	0.5	5
PKS 1622-253	0.786	794.3	-3555, 1566	9.0	2.44701(15)	<0.55	...	0.004	0.03	4
PKS 1622-29	0.815	781.6	-2354, 1570	9.3	2.830(9)	<0.50	...	0.0160	0.121	2
3C343	0.988	714.5	-3491, 2250	5.68	8.56(7)	<0.11	...	0.20	1.6	5
1637+574	0.7506(10)	811.4(5)	-8992, 3641	6.2	0.9(3)	<0.99	...	5.3	39	9
3C343.1	0.75	811.7	-3494, 3306	5.52	7.28(6)	<0.11	...	0.24	1.8	5
1642+690	0.751	810.2	-7376, 2826	8.2	1.87(5)	<0.64	< 1.3 ²	0.0041	0.030	2
1656+053	0.879	754.9	-2892, 2922	9.4	1.93(5)	<0.77	...	2.4	19	9
1730-130	0.902	745.8	-7145, 6534	11	6.7(2)	<0.27	...	0.0045	0.035	2
1741-038	1.054	567.3	...	RFI	0.0016	0.013	2
1749+701	0.770	801.5	-5764, 2998	6.9	1.3(8)	<0.78	...	0.0047	0.035	2
1803+784	0.680	844.5	-2230, 2474	6.0	2.1(2)	<0.41	...	0.0016	0.011	2
1800+440	0.663	845.1	...	RFI	0.0009	0.006	2
COINS J1815+6127	0.601(3)	887.2(1.7)	-1693, 2244	2.64	0.53(6)	7(3)	4.4 ²	0.010	0.068	3
1823+568	0.6640(10)	853.6(5)	...	RFI	0.0061	0.043	2
3C380	0.69	840.5	-3688, 4958	12.4	21.7(2)	<0.081	< 0.19 ²	1.3	9.0	3
4C+29.56	0.842(3)	771.1(1.3)	-1656, 1998	1.86	3.90(1)	<0.19	< 1.6 ²	2.9	20	3
WMAP 1849+6705	0.6570(10)	857.2(5)	...	RFI	0.0026	0.018	2
TXS 1848+283	2.56	398.99	-445, 6101	6.55	0.181(6)	<7.6
TXS 1851+488	1.250(3)	631.3(8)	...	RFI	0.005	0.04	6
1921-293	0.35263(18)	1050.11(14)	...	RFI	0.0067	0.033	2
PKS 2000-330	3.7730(10)	297.59(6)	-4352, 3697	10.2	0.16(3)	<9.5
2007+777	0.342	1058.4	-846, 970	4.2	1.01(10)	<0.64	< 1.8 ⁶	0.0048	0.023	13
PKS 2008-068	0.5470(10)	918.2(6)	-1858, 340	3.70	2.135(9)	<0.30	...	0.30	0.19	5
COINS J2022+6136	0.227	1157	-9869, 1621	7.2	1.99(15)	<0.61	< 0.36 ²	0.010	0.036	5
2059+034	1.013	705.6	...	RFI	0.0016	0.013	4
PKS 2121-01	1.158(2)	658.2(6)	-944, 20	49	1.548(7)	<6.0	< 6.9 ⁷	0.088	0.73	14
PKS 2126-15	3.2680(10)	332.80(8)	-4982, 4118	5.68	0.101(9)	<7.2	...	0.008	0.06	5
PKS 2127+04	0.99	713.8	-972, 1365	6.03	5.04(8)	<0.20	...	0.030	0.24	5
2128-123	0.501	945.3	-1527, 9545	6.3	1.84(3)	<0.59	...	0.0105	0.0633	4
PKS 2134+004	1.9320(10)	484.45(17)	...	RFI	0.002	0.017	5
2145+067	0.990	712.8	-1432, 993	14	3.355(2)	<0.68	...	0.0071	0.057	2
PKS 2149+056	0.740(10)	816.3(5)	-3595, 1873	3.39	0.507(3)	<0.98	< 5.8 ¹	0.004	0.03	3
2155-152	0.672	848.5	-2189, 1779	8.3	2.68(16)	<0.43	...	0.0072	0.051	2
2201+315	0.2950(5)	1096.8(4)	-1521, 1395	9.5	1.9(2.2)	<0.48	...	0.0054	0.024	2
2216-038	0.901	746.2	-2745, 1660	9.9	1.372(2)	<1.2	...	0.0005	0.004	15
PKS 2230+11	1.037	697.3	-3036, 2899	4.87	7.50(9)	<0.11	...	2.6	21	16
2234+282	0.795	790.3	-5071, 4060	8.2	0.597(5)	<2.1	...	0.0011	0.083	4
3C454.1	1.841	499.97	...	RFI	1.6	14	5
3C454	1.757	515.2	-1670, 897	7.49	4.87(3)	<0.24	...	0.66	5.6	5
3C454.3	0.859	763.1	-8290, 1838	9.2	13.87(11)	<0.10	...	0.0078	0.060	2
3C455	0.543	920.6	-892, 3709	2.88	4.45(5)	1.8(6)	0.42 ²	2.6	17	3
2255-282	0.92584(15)	737.69(6)	...	RFI	0.0050	0.039	4
3C459	0.22012(3)	1164.15(3)	-9191, 3515	4.9	5.23(3)	<0.16	...	1.86	6.55	17
HB89 2342+821	0.735	818.7	-3211, 3413	5.14	4.53(4)	<0.16	< 0.16 ²	0.267	1.94	3
HB89 2344+092	0.677	847.0	-5233, 2063	6.4	2.233(2)	<0.40	...	0.0092	0.065	4

Table 2 — *Continued*

Source	z	ν (MHz)	Δv (km s $^{-1}$)	rms (mJy)	Ctnm (Jy)	N_{HI} (10 20 cm $^{-2}$)	Prev. N_{HI}	Size (arcsec)	Size (kpc)	Ref.
--------	-----	----------------	-------------------------------	--------------	--------------	---	-----------------------	------------------	---------------	------

Note. — Columns list the source name, optical redshift, centroid or expected frequency for the HI 21 cm absorption line, velocity range searched (blue, red limits), spectral rms noise in the search region, the continuum flux density at the expected redshifted line frequency, the measured column density or 3σ upper limit, previously measured column densities (or upper limits), largest projected angular size and linear size, respectively, and references for the continuum source characteristics. Numbers in parentheses show uncertainties in the final digit(s). Detections and non-detections assume $f = 1$, and $T_s = 100$ K. Non-detections also assume a line width of 30 km s $^{-1}$ (Sec. 4.3). References for previous HI 21 cm observations (non-detections are converted to our standard linewidth and spin temperature to aid in comparison): 1 – Carilli et al. (1998); 2 – Vermeulen et al. (2003); 3 – Gupta et al. (2006); 4 – Ishwara-Chandra et al. (2003); 5 – Curran et al. (2013); 6 – Aditya & Kanekar (2018b); 7 – Aditya & Kanekar (2018a); 8 – Curran et al. (2017); 9 – Curran et al. (2019); 10 – Aditya et al. (2016). References for sizes: 1 – Stanghellini et al. (1990); 2 – Gurvits et al. (1999); 3 – Gupta et al. (2006); 4 – Fomalont et al. (2000); 5 – O’Dea & Baum (1997); 6 – Xu et al. (1995); 7 – Fey & Charlot (2000); 8 – Menon (1983); 9 – Murphy et al. (1993); 10 – Antonucci & Ulvestad (1985); 11 – Shen et al. (1998); 12 – Fanti et al. (2001); 13 – Fey & Charlot (1997); 14 – Xiang et al. (2005); 15 – Shen et al. (1997); 16 – Fanti et al. (1990); 17 – Morganti, Killeen, & Tadhunter (1993).

Table 3
OH 18 cm Observations and Column Density Limits

Source	<i>z</i>	1612 MHz			1667 MHz			1720 MHz			Cntrm (Jy)	N_{OH}/T_x ($10^{13} \text{ cm}^{-2} \text{ K}^{-1}$)
		ν (MHz)	Δv (km s $^{-1}$)	rms (mJy)	ν (MHz)	Δv (km s $^{-1}$)	rms (mJy)	ν (MHz)	Δv (km s $^{-1}$)	rms (mJy)		
0018+729	0.821	885.35	...	RFI	915.63	-8945, 9866	2.41	944.83	0.9244(5)	<6.0
LBQS 0106+0119	2.009	535.80	-10741, 7163	5.5	554.12	-3179, 2231	5.5	571.79	-1681, 3562	5.1	2.7(2)	<3.8
UM321	1.07481	777.05	-4688, 3492	9.1	803.62	-4357, 4894	6.1	829.25	...	RFI	1.355(18)	<8.9
3C43	1.459	655.64	-153, 1868	12.3	678.06	-3188, 491	19.1	699.69	-1257, 2514	18.2	5.25(3)	<8.5
0133+476	0.859	867.26	...	RFI	896.91	-1834, 572	3.9	925.51	-1000, 5,900	6.1	1.983(11)	<4.6
3C48	0.367	1179.4	-3967, 3659	8.1	1219.7	-3755, 3618	7.1	1258.6	-5093, 623	11.1	17.93(4)	<0.85
PKS 0201+113	3.6390	347.54	-3762, 7969	9.78	359.42	-4905, 3186	10.1	370.88	-10440, 5645	11.9	0.365(8)	<41
0212+735	2.367	478.83	...	RFI	495.21	...	RFI	511.00	...	RFI
3C066A	0.444	1116.5	...	RFI	1154.7	-6314, 1215	8.1	1191.5	-5660, 2894	5.1	2.54(14)	<7.2
B2 0218+357	0.944	829.34	-4722, 3917	6.8	857.69	...	RFI	885.05	...	RFI	1.492(4)	<78 ^a
0221+067	0.511	1067.0	...	RFI	1103.5	...	RFI	1138.7	...	RFI
4C+34.07	2.91	412.34	-10626, 7180	12.2	426.43	...	RFI	440.03	3.61(9) ^a	<77 ^a
HB89 0235+164	0.94	831.05	-5142, 4598	5.6	859.46	-3222, 6719	5.4	886.87	-11266, 903	5.6	1.0(2)	<13
PKS 0237-23	2.223	500.23	...	RFI	517.33	...	RFI	533.83
PKS 0239+108	2.694	436.45	-2064, 2710	18	451.37	...	RFI	465.76	...	RFI	1.41(14) ^a	<281 ^a
B3 0248+430	1.31	697.94	-114, 2034	7.8	721.80	-1121, 4444	7.8	744.82	...	RFI	0.782(3)	<22
0306+102	0.863	865.40	...	RFI	894.99	-9786, 297	4.1	923.53	-413, 2378	5.4	0.48210(2)	<20
OE+131	2.662	440.26	-2956, 2015	13.9	455.31	...	RFI	469.83	2.586(8) ^a	<112 ^a
PKS 0327-241	0.895	850.78	-3706, 3729	5.6	879.87	907.93	0.8660(4) ^a	<108 ^a
0336-019	0.852	870.54	...	RFI	900.30	-7791, 2032	4.4	929.01	...	RFI	2.22(8)	<46
0346-279	0.991	809.76	...	RFI	837.45	-3133, 2595	4.5	864.15	-4422, 4,182	4.1	0.98(6)	<8.6
4C+76.03	0.5985	1008.6	-751, 3081	6.32	1043.0	-1713, 2109	4.37	1076.3	...	RFI	6.243(7)	<1.4
0420-014	0.914	841.42	-3048, 2077	5.9	870.91	...	RFI	897.94	-7164, 1240	7.9	2.02(13) ^a	<49 ^a
0422+004	0.31	1230.7	-5819, 2609	4.9	1272.8	-3087, 1788	5.8	1313.4	-3337, 270	3.4	0.51(5)	<24
3C119	1.023	796.95	-4292, 2897	8.56	824.20	...	RFI	850.48	13.7(1.7) ^a	<11 ^a
0440-003	0.844	874.31	...	RFI	904.21	-6562, 3285	3.8	933.04	-3392, 142	5.7	2.60(4)	<3.4
PKS 0454-234	1.003	804.91	-10165, 2834	8.9	832.43	-4239, 6170	8.4	858.98	...	RFI	1.58(11)	<10
PKS 0457+024	2.384	476.43	...	RFI	492.72	...	RFI	508.43
0458-020	2.286	490.64	...	RFI	507.41	...	RFI	523.59	...	RFI
3C138	0.76	916.04	-1522, 2154	6.61	947.36	-3922, 2256	6.84	977.57	-471, 2862	7.91	10.5(4)	<1.4
PKS 0528-250	2.813	422.82	-3173, 3329	2.84	437.28	-1442, 12882	11.8	451.23	1.5(2.9)	<19
PKS 0539-057	0.839	876.69	...	RFI	906.67	-6194, 4,023	4.5	935.58	-4909, 3326	6.7	0.91(9)	<12
3C147	0.55	1040.2	-4914, 2349	9.1	1075.7	-1361, 2652	9.2	1110.0	-4208, 788	11.2	26.2(6)	<0.68
0605-085	0.872	861.23	...	RFI	890.68	-7276, 1846	6.5	919.09	-6724, 3551	5.6	2.853(14)	<5.4
0607-157	0.324	1217.7	-3768, 5588	10	1259.3	-4729, 270	5.7	1299.5	-837, 737	10.2	2.30(3)	<5.2
HB89 0636+680	3.1800	385.70	-9194, 13121	4.73	398.89	-10496, 9695	7.69	411.61	-12972, 6621	7.99	0.128(2)	<173
B2 0711+35	1.62	615.36	...	RFI	636.40	...	RFI	656.69
0735+178	0.424	1132.2	...	RFI	1170.9	-6427, 3814	3.8	1208.2	-4904, 5021	4.6	2.15(5)	<4.0
0736+017	0.191	1355.5	-4279, 5908	3.3	1401.8	-1935, 7488	3.6	1446.5	...	RFI	2.53(3)	<3.2
B2 0738+31	0.63139	988.26	-2886, 869	2.71	1022.1	-1865, 3447	2.22	1054.6	1.68(7)	<2.7
PKS 0742+10	2.624	444.88	...	RFI	490.09	...	RFI	474.76	...	RFI
PKS 0743-006	0.994	808.54	-2083, 2225	4.79	836.19	-3203, 3073	5.6	862.85	-2149, 981	15.9	0.672(6)	<16
3C186	1.067	779.99	-5121, 5583	2.89	806.66	-2110, 1973	6.71	832.38	-6641, 2892	3.01	2.465(19)	<5.3
PKS 0745+241	0.4092	1144.1	-2679, 2352	4.5	1183.2	...	RFI	1220.9	1.007(10) ^a	<92 ^a
0748+126	0.889	853.48	...	RFI	882.67	...	RFI	910.82	-4208, 762	8.6	1.49(4) ^b	<120 ^b
COINS J0753+4231	3.58925	351.31	-5317, 13086	6.39	363.32	-3452, 6552	6.59	374.90	-3395, 1195	6.81	0.7602(2)	<13
HB89 0754+100	0.266	1273.5	-3888, 1997	3.8	1317.0	-4774, 4559	3.7	1359.0	-3082, 5301	3.5	1.1(8)	<6.7
SBS 0804+499	1.43	663.47	...	RFI	686.16	...	RFI	708.04	...	RFI
PKS 0823+033	0.506	1070.5	-2930, 4071	4.4	1107.1	-3752, 3288	4.6	1142.5	-506, 3005	4.2	1.3(6)	<8.3
PKS 0823-223	0.91	844.10	-2593, 2451	6.4	872.96	...	RFI	900.80	-6656, 1531	5.8	0.61(6) ^a	<177 ^a
0828+493	0.548	1041.5	-2737, 2733	5.1	1077.1	-2476, 4761	4.8	1111.5	-4733, 1471	3.6	0.92(14)	<10
0836+710	2.172	508.27	...	RFI	525.65	...	RFI	542.41	...	RFI

Table 3 — *Continued*

Source	<i>z</i>	1612 MHz			1667 MHz			1720 MHz			Cntm	N_{OH}/T_x (10^{13} cm $^{-2}$ K $^{-1}$)
		ν (MHz)	Δv (km s $^{-1}$)	rms (mJy)	ν (MHz)	Δv (km s $^{-1}$)	rms (mJy)	ν (MHz)	Δv (km s $^{-1}$)	rms (mJy)		
TXS 0902+490	2.6887	437.07	-6130, 1099	5.38	452.02	...	RFI	466.43	...	RFI	0.907(3) ^a	<124 ^a
0906+015	1.024	796.56	-2989, 9129	7.8	823.79	-6298, 1890	7.9	850.06	-42, 4008	6.8	1.33(19)	<11
3C216	0.6703	965.23	998.24	-8938, 2114	1.5	1030.01	-3762, 3223	7.1	5.53(4)	<0.57
0917+449	2.1899	505.42	...	RFI	522.70	...	RFI	539.37	...	RFI
0919-260	2.3	488.55	...	RFI	505.26	-83, 1934	18	521.37	...	RFI	0.91(11)	<42
0923+392	0.6952	951.06	-1590, 1090	6.7	983.58	-9578, 694	5.7	1014.9	-5334, 5004	5.5	3.0(2)	<4.1
0925-203	0.34741	1196.5	-4257, 3764	4.5	1237.5	-3899, 3857	4.9	1276.9	-4849, 4077	3.1	0.83(8)	<13
HB89 0954+556	0.896	850.33	...	6.5	879.41	...	RFI	907.45	...	6.1	4.20(16) ^a	<26 ^a
1004+141	2.707	434.92	...	RFI	449.79	...	RFI	464.13	-2629, 2668	8.9	1.243(13) ^b	<147 ^b
3C237	0.87	862.16	...	RFI	891.64	-579, 2310	3.41	920.07	-1792, 2049	3.56	8.38(5)	<0.95
PKS 1034-293	0.312	1228.8	-4432, 9474	3.7	1270.9	-4753, 3032	5.6	1311.4	-5857, 3287	2.9	1.09(11)	<11
1055+018	0.888	853.94	-93, 5524	10.2	883.14	...	RFI	911.30	-3883, 4111	8.3	3.668(13) ^a	<61 ^a
1116+128	2.118	515.25	...	RFI	532.87	...	RFI	549.87	...	RFI
PKS 1124-186	1.05	786.45	-6650, 10351	6	813.35	-7318, 4845	3.6	839.28	-7364, 565	4.2	0.48(4)	<15
B3 1144+402	1.088	772.14	-8060, 5374	5.1	798.54	-5277, 6023	4.5	824.01	-7855, 4042	6.8	0.5286(4)	<17
FBQS J1159+2914	0.7245	934.9	-5702, 760	6.4	966.87	-4430, 5238	5.6	997.70	-5694, 7502	7	2.12(3)	<5.8
1202-262	0.789	901.19	-8552, 3324	10.1	932.01	-7042, 2189	8.4	961.73	-4231, 4217	6.7	1.9640(9)	<9.7
1222+037	0.9556	824.42	-5048, 3716	5.6	852.61	-595, 4925	4.3	879.80	...	RFI	0.94(11)	<8.5
PG 1222+216	0.432	1125.9	...	RFI	1164.4	-6088, 3182	3.9	1201.45	-5118, 3615	3.3	1.90(9)	<4.6
3C273	0.15834	1391.9	-3910, 5567	9.1	1439.4	-1158, 3840	7.1	1485.3	44.90(8)	<0.34
COINS J1244+4048	0.813	889.26	...	RFI	919.67	-1708, 1731	2.77	949.00	-2579, 2558	2.78	1.54(3)	<4.1
3C279	0.5362	1049.5	-1859, 5568	4.7	1085.4	...	RFI	1120.0	-538, 1604	4.6	10.6(2) ^a	<7.9 ^a
1308+326	0.996	807.73	...	RFI	835.35	-4217, 3894	6.5	861.99	...	RFI	1.17(2)	<11
3C287	1.055	784.54	-1719, 1873	3.98	811.37	-1315, 2110	4.33	837.24	-4930, 419	7.41	9.6(3)	<0.87
3C286	0.8494	871.76	...	RFI	901.57	-4224, 3876	6.55	930.32	18.04(9)	<2.0
B3 1355+441	0.646	979.48	-3635, 2832	5.61	1013.0	-3173, 5706	1.97	1045.3	-4136, 3952	1.92	0.58460(7)	<7.0
1418+546	0.1526	1398.8	-4120, 6168	3.2	1446.6	1492.7	0.92(7)	<71 ^a
3C309.1	0.905	846.32	-1603, 3229	9.63	875.25	...	RFI	903.17	-3188, 2305	10.1	10.35(5) ^a	<20 ^a
1504-166	0.876	859.40	-3070, 6697	7.7	888.78	...	RFI	917.13	2.9(2) ^a	<58 ^a
3C318	1.574	626.35	...	RFI	647.77	...	RFI	668.43
COINS J1546+0026	0.55	1040.2	-3473, 4136	3.3	1075.7	-2280, 3517	4.09	1110.0	-2290, 707	2.16	1.99(1)	<4.0
PKS 1622-253	0.786	902.70	...	RFI	933.57	...	RFI	963.34	...	RFI
PKS 1622-29	0.815	888.28	...	RFI	918.66	...	RFI	947.95	...	RFI
3C343	0.988	810.98	-646, 3490	5.47	838.71	-4429, 2920	6.68	865.46	7.67(7)	<1.6
1637+574	0.7506	920.96	-567, 4804	3.6	952.45	982.82	0.9(3) ^a	<83 ^a
3C343.1	0.75	921.27	-744, 1362	5.87	952.78	-1425, 1633	8.71	983.16	-2476, 3278	9.95	6.39(5)	<3.0
1642+690	0.751	920.75	-505, 6691	4.8	952.23	982.60	1.62(3) ^a	<61 ^a
1656+053	0.879	858.03	-340, 6438	6.3	887.37	...	RFI	915.66	...	RFI	1.84(5) ^a	<76 ^a
1730-130	0.902	847.65	-2458, 2989	9.5	876.63	...	RFI	904.59	...	RFI	6.6(2) ^a	<24 ^a
1741-038	1.054	784.92	-4078, 7915	10.6	811.76	-8139, 5747	5.6	837.65	-5995, 662	7.8	1.402(8)	<7.8
1749+701	0.77	910.86	-3895, 5485	4.8	942.01	972.05	1.3(7) ^a	<76 ^a
COINS J1815+6127	0.601	1007.0	-957, 1428	2.09	1041.5	-2672, 1721	2.07	1074.7	-800, 234	3.19	0.50(5)	<8.4
1823+568	0.664	968.89	-1643, 6711	4.6	1002.0	-4542, 3027	5.3	1034.0	...	RFI	1.62(5)	<6.9
3C380	0.69	953.98	-197, 2084	3.52	985.44	-2666, 1776	4.6	1018.1	-1954, 1874	5.83	18.89(17)	<0.52
4C+29.56	0.842	875.26	...	RFI	905.19	...	RFI	934.06
WMAP J1849+6705	0.657	972.98	-6507, 7328	4.7	1006.3	-3798, 5736	5.8	1038.3	-479, 676	4.9	0.6(1.3)	<20
TXS 1848+283	2.56	452.87	-461, 5279	13.6	468.36	...	RFI	483.29	0.188(6) ^a	<1640 ^a
PKS 2000-330	3.7730	337.78	-7046, 3614	11.5	349.33	-3587, 4514	11.6	360.47	-4066, 4234	9.19	0.18(2)	<109
PKS 2008-068	0.5470	1042.2	-240, 2435	6.67	1077.8	...	RFI	1112.2	2.307(10) ^a	<51 ^a
COINS J2022+6136	0.227	1314.0	-5713, 4098	4.8	1358.9	-2892, 7256	4.3	1402.2	-3800, 7959	4.3	2.18(17)	<4.6
2059+034	1.013	800.91	-5387, 6704	6.4	828.30	-3730, 6550	4.8	854.71	-698, 6352	5.6	0.342(3)	<27
PKS 2126-15	3.2680	377.75	-4366, 3110	5.62	390.67	-4405, 2563	8.47	403.12	0.124(8)	<204
PKS 2127+04	0.99	810.17	-1633, 2659	6.08	837.87	-4812, 5707	8.27	864.59	...	RFI	4.80(6)	<3.2

Table 3 — *Continued*

Source	z	1612 MHz			1667 MHz			1720 MHz			Cntrm	N_{OH}/T_x ($10^{13} \text{ cm}^{-2} \text{ K}^{-1}$)
		ν (MHz)	Δv (km s $^{-1}$)	rms (mJy)	ν (MHz)	Δv (km s $^{-1}$)	rms (mJy)	ν (MHz)	Δv (km s $^{-1}$)	rms (mJy)		
2128–123	0.501	1074.1	...	RFI	1110.8	...	RFI	1146.2	...	RFI
PKS 2135–209	0.63634	985.27	−2832, 2795	4.34	1019.0	−1620, 4348	8.22	1051.5	...	RFI	4.9(6)	<3.4
2145+067	0.990	810.17	−4601, 4,317	5.7	837.87	−4663, 597	5.2	864.59	...	RFI	3.304(2)	<3.0
2155−152	0.672	964.25	−2564, 5364	6.1	997.22	−9252, 5599	5.1	1029.0	−6693, 9330	3.9	2.79(18)	<3.8
2201+315	0.295	1245.0	−2175, 3604	5.3	1287.5	−3368, 6877	5.2	1328.6	−3025, 6452	3.6	1(3)	<5.6
2216−038	0.901	848.10	−956, 3852	6.3	877.10	...	RFI	905.07	...	RFI	1.3460(3) ^a	<78 ^a
PKS 2230+11	1.037	791.47	−1321, 1342	5.06	818.54	−3388, 3392	12.2	844.64	−2591, 1671	4.44	7.34(7)	<2.1
2234+282	0.795	898.18	...	RFI	928.89	−3618, 6097	5.6	958.51	−4469, 3851	4.5	0.626(6)	<20
3C454	1.757	584.78	...	RFI	604.77	...	RFI	624.06
3C454.3	0.859	867.26	...	RFI	896.91	...	RFI	925.51
3C455	0.543	1044.9	...	RFI	1080.6	...	RFI	1115.1
2255−282	0.92548	837.31	...	RFI	865.94	...	RFI	893.56	−9961, 1785	4.4	1.1440(5) ^b	<81 ^b
3C459	0.22012	1321.4	−4113, 5643	4.4	1366.6	−1546, 8940	4.2	1410.1	−2055, 3132	2.9	4.50(3)	<2.1
HB89 2342+821	0.735	929.24	−3036, 3539	4.3	961.01	−4314, 3017	6.12	991.66	−3579, 2343	4.7	4.32(4)	<3.0
HB89 2344+092	0.677	961.38	−3281, 4421	4.6	994.25	−5352, 4267	4.4	1026.0	−2350, 7585	4.2	2.198(2)	<4.2

Note. — Columns list the source name, the optical redshift, and the expected frequency, the velocity range searched (blue, red limits), and the spectral rms noise for each of the 1612, 1667, and 1720 MHz OH lines. The final two columns list the continuum flux density expected at the redshifted 1667 MHz OH line, and the 3σ column density limit for that line, unless otherwise noted (Sec. 4.3). Numbers in parentheses show uncertainties in the final digit(s).

^a Since the 1667 (and 1665) MHz line was not observable due to RFI, we use the 1612 MHz line to obtain an upper limit on the OH column density. The interpolated continuum corresponds to the redshifted frequency of this line.

^b The interpolated continuum and OH column density limit are based on the 1720 MHz OH line.

Table 4
Intrinsic HI 21 cm Absorption Line Measurements and Derived Quantities

Source	Comp.	ν (MHz)	z	Ctnm (Jy)	FWHM (kHz)	FWHM (km s $^{-1}$)	Depth (mJy)	τ (10 $^{-2}$)	N_{HI} (10 20 cm $^{-2}$)
COINS J0111+3906	1	851.373(5)	0.668371(10)	0.153(2)	190(10)	67(4)	85(2)	81 $^{+2}_{-4}$	104 $^{+7}_{-8}$
	2	851.173(9)	0.668763(18)	0.153(2)	142(17)	50(6)	34(3)	25 $^{+2}_{-3}$	24 $^{+3}_{-4}$
	Tot	851.3278	0.6685	0.153(2)	180(20)	63(7)	70(8)	61(12)	74(13)
4C+76.03	1	887.643(3)	0.600199(5)	6.618(7)	132(10)	45(3)	114(8)	1.74 $^{+0.12}_{-0.12}$	1.48 $^{+0.14}_{-0.15}$
	2	887.69(3)	0.60011(5)	6.618(7)	559(90)	189(29)	36(6)	0.53 $^{+0.09}_{-0.10}$	1.9 $^{+0.4}_{-0.5}$
	Tot	887.648	0.60019	6.618(7)	199(79)	67.2(27)	165(6)	2.9(1.1)	3.7(1.1)
PKS 0500+019	1	896.324(9)	0.58470(2)	1.57(7)	284(20)	95(7)	49(3)	3.2 $^{+0.1}_{-0.3}$	5.9 $^{+0.5}_{-0.7}$
	2	895.878(9)	0.58549(2)	1.57(7)	77(21)	26(7)	25(6)	1.6 $^{+0.3}_{-0.4}$	0.79 $^{+0.2}_{-0.3}$
	Tot	896.299	0.5847	1.57(7)	372(47)	125(16)	58(7)	3.0(4)	7.1(1.3)
3C216	1	850.16(2)	0.67075(4)	6.39(4)	214(47)	75(20)	12(3)	0.19 $^{+0.04}_{-0.05}$	0.28 $^{+0.09}_{-0.10}$
	2	850.37(3)	0.67034(6)	6.39(4)	701(43)	247(15)	23.4(1.9)	0.37 $^{+0.02}_{-0.03}$	1.74 $^{+0.17}_{-0.19}$
	Tot	850.336	0.6704	6.39 (4)	613(95)	216(33)	37(4)	0.44(7)	1.8(4)
COINS J1815+6127	1	885.945(8)	0.603266(14)	0.53(6)	219(19)	71(6)	21.9(1.5)	4.21 $^{+0.03}_{-0.08}$	5.7 $^{+0.7}_{-1.2}$
	2	886.24(2)	0.60273(4)	0.53(6)	167(56)	56(19)	6.6(6)	1.250 $^{+0.011}_{-0.02}$	1.4 $^{+0.5}_{-0.5}$
	Tot	885.978	0.6032	0.53	296(88)	100(30)	25(3)	3.7(1.1)	7(3)
3C455	1	920.51(1)	0.54313(3)	4.45(5)	309(47)	101(15)	9.2(1.4)	0.21 $^{+0.03}_{-0.04}$	0.40 $^{+0.08}_{-0.09}$
	2	920.34(3)	0.54335(5)	4.45(5)	829(60)	270(20)	10.3(1.4)	0.23 $^{+0.02}_{-0.03}$	1.20 $^{+0.16}_{-0.19}$
	3	919.55(1)	0.54467(2)	4.45(5)	153(28)	50(9)	6.5(9)	0.15 $^{+0.01}_{-0.02}$	0.14 $^{+0.03}_{-0.03}$
	Tot	920.376	0.5433	4.45(5)	510(150)	170(50)	20(2)	0.57(17)	1.8(6)

Note. — Sources for which 21 cm absorption is detected. Columns list the source name, Gaussian component, central frequency, redshift, continuum flux density, FWHM width of the line (rest-frame), line depth, peak optical depth, and derived column density corresponding to each individual Gaussian component. For rows labeled with Tot, these measurements correspond to the direct integration for each absorption profile. Numbers in parentheses show statistical uncertainties in the final digit(s).

Table 5
UV, Optical, Near-IR, and Radio Properties

Source	B (mag)	V (mag)	R (mag)	K (mag)	z	D_L (Mpc)	$\log L_{\text{UV}}$ (W Hz $^{-1}$)	$\log L_{\text{Radio}}$ (W Hz $^{-1}$)	References
0018+729	20.9(i-band)	...	0.821	5188.7	...	27.25	1
COINS J0111+3906	22.00	16.69	0.66847	4023.5	20.40	26.21	2,3
UM321	16.72	16.44	16.30	14.41	1.07481	7303.7	24.39	27.60	4,5,6
3C43	21.38	...	19.70	20.0	1.459	10635	22.27	28.52	7,8
3C48	16.62	16.2	...	12.72	0.367	1950.7	23.07	27.83	7,6
0138-097	17.1	...	17.0	14.40	0.733	4508.2	24.13	27.03	10,6
PKS 0201+113	19.5	16.8	3.6390	32616	24.08	27.96	11
B2 0218+357	...	19.60	...	14.84	0.944	6173.8	22.38	27.56	5,6
3C066A	12.85(H-band)	12.02	0.444	2446.5	23.75	27.15	12
0221+067	19.65	18.97	17.78	14.41	0.511	2897.7	21.18	26.81	8,5,13
HB89 0235+164	...	19.0	16.89	10.49	0.940	6141.2	19.02	27.39	14,15,16
PKS 0237-23	...	16.6	...	13.6	2.223	17922	24.88	28.61	17,18
0306+102	...	21.2	19.91	15.19	0.863	5520.8	19.78	26.98	19,5,6
NGC 1275	14.80	13.03	12.62	11.30	0.01765	75.6	19.06	25.19	20,21,22,6
OE+131	...	19.0	19.0	15.38	2.662	22347	24.27	28.64	7,18,6
PKS 0327-241	19.31	...	0.895	5776.9	...	27.30	5
0336-019	18.32	17.77	17.33	14.49	0.852	5433.4	23.13	27.63	4,5,6
0346-279	17.72	14.68	0.991	6559.7	23.38	27.43	5,23
4C+76.03	21.2	...	0.5985	3512.8	...	27.79	24
3C119	20.0	15.02	1.023	6825.3	21.91	28.59	7,6
0440-003	18.35	17.98	17.85	...	0.844	5370.0	23.46	27.65	4,5
PKS 0457+024	18.78	18.5	2.384	19528	24.23	27.72	4
PKS 0500+019	22.5	21.35	20.68	15.43	0.58457	3413.1	20.28	27.14	25,26,27
3C138	19.37	18.84	18.48	15.43	0.76	4714.7	22.65	28.24	28,29,6
PKS 0528-250	18.16	15.37	2.813	23900	24.63	28.44	30
PKS 0539-057	...	19.9	...	14.41	0.839	5330.5	21.93	27.23	31,6
3C147	18.45	17.8	17.21	14.56	0.55	3168.8	22.33	28.36	28,49,6
B3 0552+398	18.62	18.0	18.03	14.68	2.365	19338	24.29	27.81	8,18,6
0605-085	...	18.5	17.70	12.41	0.872	5592.6	22.02	27.74	14,5,6
HB89 0636+680	17.59	...	16.58	13.75	3.1800	27729	25.04	27.41	8,6
B2 0711+35	...	17.0	1.62	12116	...	27.77	18
0735+178	16.28	15.65	15.29	10.34	0.424	2315.3	23.14	26.99	32,33

Table 5 — *Continued*

Source	B (mag)	V (mag)	R (mag)	K (mag)	<i>z</i>	D _L (Mpc)	log <i>L</i> _{UV} (W Hz ⁻¹)	log <i>L</i> _{Radio} (W Hz ⁻¹)	References
0736+017	14.90	14.34	13.39	12.96	0.189410	921.8	22.23	26.33	34,35
B2 0738+31	16.52	16.1	16.32	16.1	0.6314	3750.9	24.16	27.19	8,36,37
PKS 0742+10	24	23.8	23.1	...	2.624	21857	22.23	28.39	38
3C186	18.50	17.97	17.67	15.68	1.0670	7194	23.42	27.95	32,41
PKS 0745+241	19.65	18.80	18.31	13.90	0.4092	2219.3	21.4	26.64	32,6
COINS J0753+4231	19.44	18.26	17.59	15.47	3.5892	32081	24.66	28.31	32,42
HB89 0754+100	15.76	15.22	14.91	11.71	0.2660	1341.3	23.01	26.25	32,33
PKS 0823+033	17.95	17.32	16.96	14.42	0.506	2863.6	22.67	26.92	32,6
PKS 0823–223	...	16.2	15.4	12.19	0.910	5897.8	23.01	27.15	36,39,40
0828+493	20.46	19.61	19.12	14.83	0.548	3154.5	21.44	26.89	32,6
PKS 0858–279	...	17.0	...	13.59	2.152	17220	24.65	27.99	18,6
TXS 0902+490	17.74	17.49	17.35	15.08	2.6887	22621	24.71	28.20	32,6
3C216	18.96	19.05	18.22	14.86	0.6703	4037.1	22.79	27.87	43,32,41
0919–260	18.05	...	18.01	15.04	2.300	18688	24.54	28.04	30,5
0923+392	17.07	17.02	16.79	14.16	0.6952	4222.7	23.96	27.60	12
0925–203	16.00	13.78	0.34741	1832.4	23.32	26.42	5,35
HB89 0954+556	18.30	17.71	17.38	14.19	0.896	5784.9	23.24	27.96	32,6
HB89 0954+658	15.75	12.43	0.368	1957.0	22.99	26.41	46,40
1004+141	18.97	18.53	18.28	...	2.707	22808	24.28	28.34	32
3C237	21.49	21.14	20.95	...	0.87	5576.6	20.89	28.27	32
PKS 1034–293	18.83	18.26	17.54	12.71	0.312	1612.8	21.43	26.4	13,5,33
1055+018	18.19	17.73	16.68	14.12	0.888	5720.7	22.87	27.89	4,5,6
PKS 1124–186	19.23	12.28	1.050	7051.1	21.65	27.13	5,6
B3 1144+402	18.97	18.25	18.12	13.53	1.0880	7371.3	23.24	27.27	32,6
FBQS J1159+2914	18.67	18.12	17.93	11.47	0.7245	4450.9	23.00	27.49	32,6
1202–262	15.97(H-band)	15.04	0.789	4938.8	22.85	27.56	6
B2 1219+28	15.72	15.31	14.72	11.85	0.102	464.6	21.89	25.33	32,15
1222+037	19.23	18.79	18.5	...	0.9556	6268.6	23.07	27.31	4,10
PG 1222+216	15.976	15.98	15.99	13.07	0.4320	2367.6	24.27	26.98	32,6
3C273	12.99	12.81	12.71	9.81	0.15834	748.7	24.28	27.44	12,15,35
COINS J1244+4048	20.68	20.22	19.97	...	0.813	5126	21.16	27.45	32
3C279	18.01	17.75	17.11	12.58	0.5362	3072.1	22.79	27.91	28,16
3C287	18.67	18.12	17.80	15.50	1.055	7093	23.32	28.49	32,6
3C286	17.51	17.25	16.5	14.88	0.8494	5412.8	25.67	28.57	44,45,10,6
HB89 1333+459	18.00	17.91	17.89	15.04	2.4490	20183	24.55	27.16	32,6
1354+195	16.34	16.09	15.92	13.89	0.720	4409.6	24.17	27.63	32,6
1418+546	16.27	15.63	15.27	11.43	0.1526	718.9	22.06	25.68	32,6
3C309.1	16.4	14.72	0.905	5857.4	24.45	28.39	10,6
1504–166	20.28	19.75	17.00	14.01	0.876	5624.6	20.77	27.72	13,31,8
3C318	21.14	20.18	19.64	...	1.5740	11689	22.38	28.6	32
COINS J1546+0026	19.73	18.9	20.1	15.43	0.55	3168.5	23.28	27.2	4,6
PKS 1622–253	20.95	...	19.60	14.86	0.786	4915.5	21.27	27.6	8,5,6
PKS 1622–29	15.06(H-band)	14.15	0.815	5141.6	23.30	27.69	6
3C343	21.26	...	20.6	...	0.988	6534.9	22.34	28.34	8,18
1637+574	17.11	16.9	16.94	13.54	0.7506	4642.6	24.09	27.14	8,31,5,6
3C343.1	20.8	...	0.75	4638.0	...	28.03	18
1642+690	...	19.2	19.38	...	0.751	4642.6	22.54	27.39	14,5
1656+053	17.33	16.55	16.21	14.06	0.879	5648.5	23.88	27.59	13,47,5,35
1730–130	...	19.5	18.78	14.29	0.902	5833.2	23.05	28.16	31,5,6
1749+701	...	17.0	15.48	13.03	0.770	4791.7	24.21	27.31	14,5,40
1803+784	...	15.9	15.46	14.15	0.680	4109.2	24.51	27.4	31,5,48
COINS J1815+6127	21.27	...	19.12	...	0.601	3530.8	20.53	26.69	8
3C380	16.26	...	16.86	14.25	0.69	4183.8	24.99	28.43	8,29,41
4C+29.56	21.92	...	20.2	...	0.842	5354.2	21.15	27.86	8
TXS 1848+283	18.19	18.09	17.12	14.62	2.56	21307	24.52	26.42	49,8,6
PKS 2000–330	18.34	17.05	16.92	15.10	3.7730	34060	25.31	27.66	30,13
2007+777	17.36	13.83	0.342	1795.4	22.19	26.46	40,5
PKS 2008–068	21.3	...	0.5470	3147.5	...	27.21	7
COINS J2022+6136	19.83	...	17.58	14.28	0.227	1119.4	19.59	26.39	8,5,6
PKS 2121–01	23.3	18.18	1.158	7968.8	20.72	27.74	50
PKS 2126–15	17.63	16.92	16.63	14.25	3.2680	28658	25.18	27.37	30,13
PKS 2127+04	22.21	...	0.99	6551.5	...	28.11	50
2128–123	16.15	15.97	15.79	13.33	0.501	2829.4	23.97	27.06	12
2145+067	16.63	16.25	15.06	13.48	0.990	6551.5	23.61	27.94	4,5,13
PKS 2149+056	23.7	22.05	20.85	17.17	0.740	4561.5	19.35	26.86	13
2155–152	18.42	18.3	17.79	14.46	0.672	4049.7	23.20	27.5	15,31,5,33
2201+315	15.52	15.46	14.33	12.34	0.2950	1511.2	22.83	26.61	8,31,5,6
2216–038	17.36	16.81	16.15	14.07	0.901	5825.2	23.43	27.47	4,5,35
PKS 2230+11	17.75	17.33	...	13.77	1.037	6942.2	23.72	28.33	45,6
2234+282	18.94	...	17.60	14.87	0.795	4985.4	22.53	27.0	8,5,6
3C454	18.64	18.52	1.757	13402	24.09	28.58	4
3C454.3	16.17	15.70	15.22	12.95	0.859	5489.0	24.02	28.43	4,5,33
3C455	19.54	19.59	19.19	13.00	0.543	3119.5	22.69	27.53	8,32,29,6
3C459	18.31	17.44	16.78	13.99	0.22012	1081.1	21.00	26.78	51,52,6
HB89 2342+821	21.77	...	20.22	15.85	0.735	4523.4	21.13	27.81	8,24,53

Table 5 — *Continued*

Source	<i>B</i> (mag)	<i>V</i> (mag)	<i>R</i> (mag)	<i>K</i> (mag)	<i>z</i>	<i>D</i> _L (Mpc)	$\log L_{\text{UV}}$ (W Hz ⁻¹)	$\log L_{\text{Radio}}$ (W Hz ⁻¹)	References
HB89 2344+092	15.96	...	14.99	13.55	0.677	4086.8	24.57	27.43	8,5,6

Note. — Columns list the source name, optical and near-IR magnitudes, luminosity distance calculated according to Wright (2006), specific UV and 21 cm radio luminosity in the host galaxy reference frame, and references for the magnitudes. For sources with only one magnitude listed, we do not calculate a UV luminosity.

Optical band magnitudes references: 1 – Stanghellini et al. (1993); 2 – Healey et al. (2008); 3 – Stickel & Kuehr (1996); 4 – Wills & Lynds (1978); 5 – Healey et al. (2008); 6 – 2MASS; Skrutskie et al. (2006); 7 – Snellen et al. (2002); 8 – SuperCOSMOS Sky Survey; Hambly et al. (2001); 9 – Sandage (1965); 10 – Atlee & Gould (2007); 11 – Kuhn (2004); 12 – Elvis et al. (1994); 13 – Francis et al. (2000); 14 – Kellermann et al. (1998); 15 – Odell et al. (1978a); 16 – O’Dell et al. (1978); 17 – Glass (1981); 18 – O’Dea et al. (1991); 19 – Sbarufatti et al. (2005); 20 – McAlary et al. (1983); 21 – Godwin et al. (1977); 22 – Gardner & Whiteoak (1978); 23 – Wright, Ables & Allen (1983); 24 – Schmitt & Kinney (1996); 25 – Drinkwater et al. (1997); 26 – Cody & Braun (2003); 27 – Curran & Whiting (2010); 28 – Sandage et al. (1965a); 29 – de Vries et al. (1997b); 30 – Ellison, Hall, & Lira (2005); 31 – Lister & Homan (2005); 32 – SDSS DR6; Adelman-McCarthy et al. (2008); 33 – Allen, Ward & Hyland (1982); 34 – Ramírez et al. (2004); 35 – Hyland & Allen (1982); 36 – Rao et al. (2006); 37 – Chun et al. (2006); 38 – Labiano et al. (2007); 39 – Sbarufatti et al. (2009); 40 – Chen et al. (2005); 41 – Simpson & Rawlings (2000); 42 – Jorgenson et al. (2006); 43 – Carballo et al. (1999); 44 – Matthews & Sandage (1963); 45 – Sandage & Wyndham (1965b); 46 – Fiorucci, Ciprini, & Tosti (2004); 47 – Tapia et al. (1976); 48 – Kotilainen et al. (2005); 49 – Ojha et al. (2009); 50 – de Vries et al. (2000); 51 – Smith & Heckman (1989); 52 – Drake et al. (2004); 53 – de Vries et al. (1998).

APPENDIX

We show the normalized spectra for the 102 RFI-free sources searched for intrinsic HI 21 cm (Figure 14) and intrinsic OH 18 cm absorption in sources with known OH 21 cm absorption (Figure 15). The observable velocity span for each source is a few thousand km s⁻¹ above/below with respect to the systemic velocity of the host galaxy and is typically determined by the RFI conditions rather than the spectral bandwidth. Table 2 lists the measured upper limits to the column densities for the 21 cm absorption line search. Table 3 lists the upper limits for the OH absorption line search.

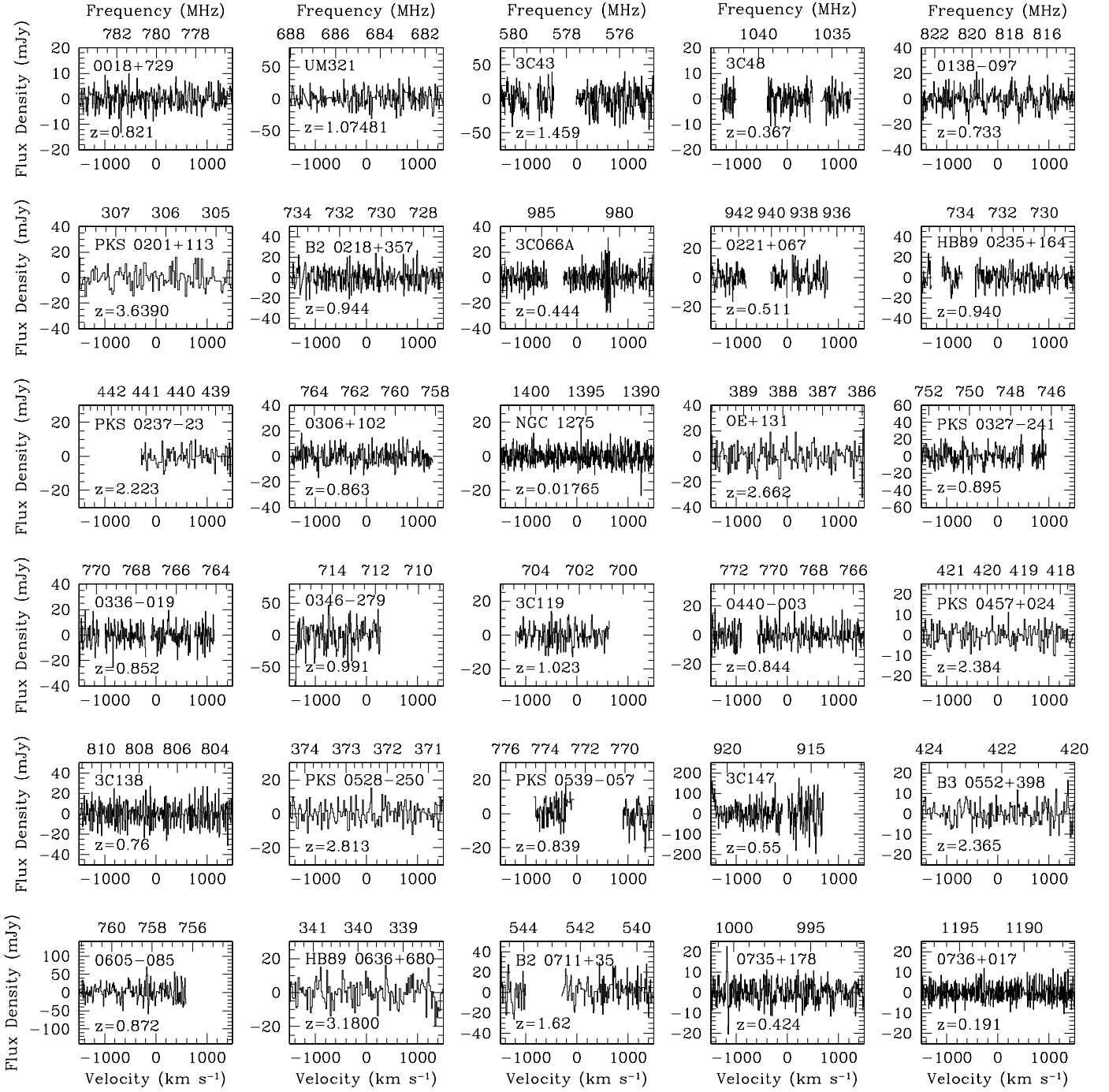
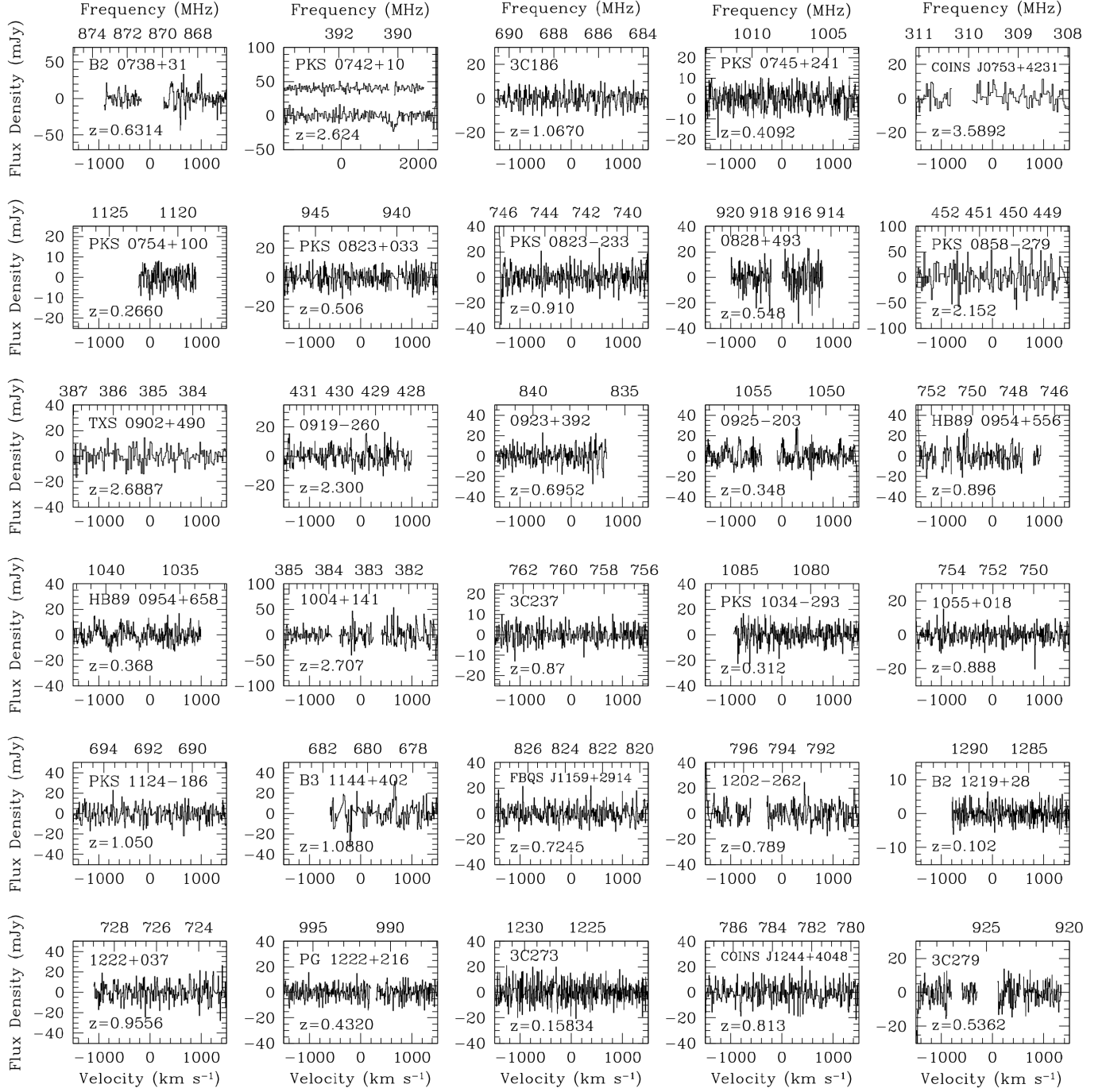
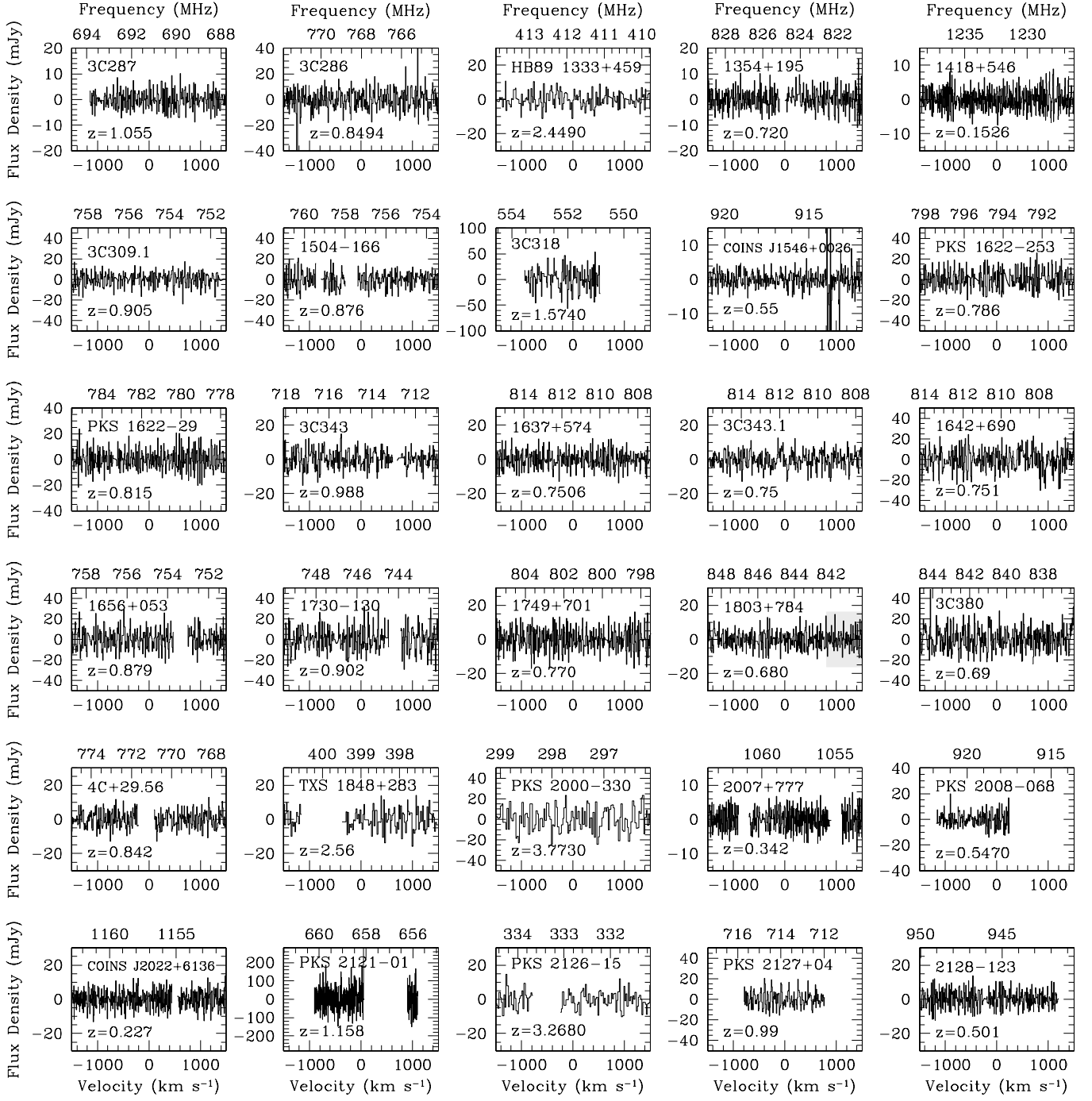


Figure 14. RFI-free sources not detected in HI 21 cm absorption. The velocity scale is in the rest frame of each object, defined by the heliocentric optical redshift of each radio source (Table 1). Spectral regions lost to radio frequency interference are not plotted. Each spectrum spans ± 1500 km s⁻¹ except for PKS 0742+10, where the x-axis has been shifted to show the feature that arises at $z = 2.64$. The upper spectrum in PKS 0742+10 shows the Curran et al. (2013) data, supporting our non-detection interpretation of the possible absorption feature.

**Figure 14.** con't.

**Figure 14.** con't.

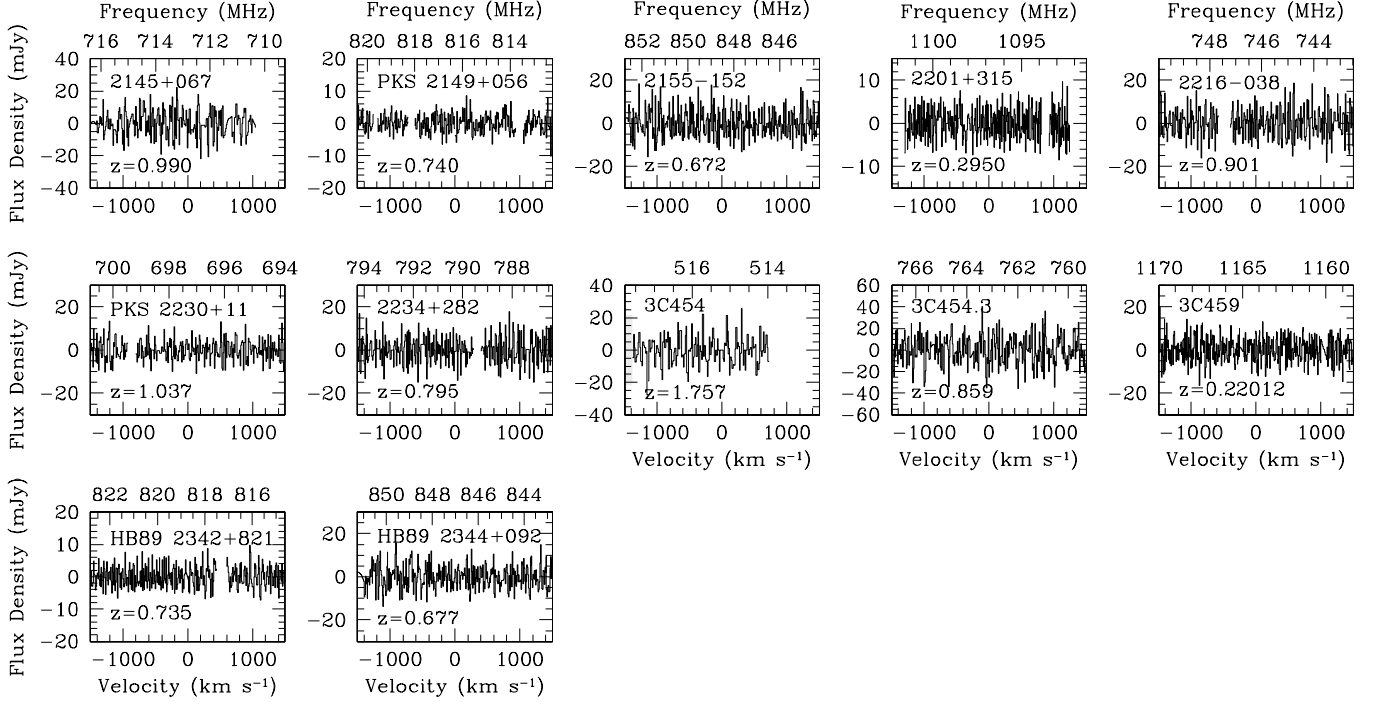


Figure 14. con't.

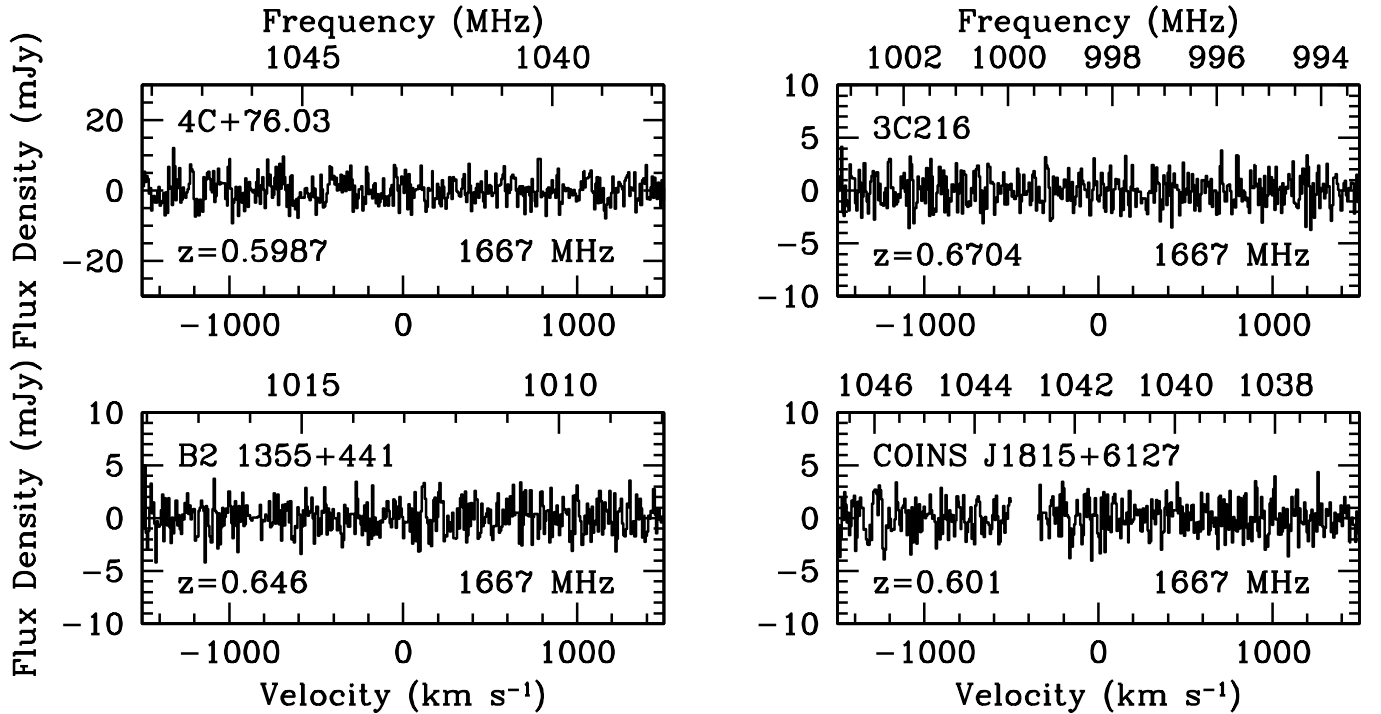


Figure 15. OH 1667 MHz spectra of the four RFI-free intrinsic HI 21 cm absorption line systems searched for OH. The velocity scale is in the rest-frame of each source, defined by the redshift of the 21 cm absorber. Spectral regions lost to radio frequency interference are omitted.